SMA Observations of Arp 299

SMA Observations of the Local Galaxy Merger Arp 299

By

Kazimierz Sliwa, B.Sc.

A Thesis

Submitted to the School of Graduate Studies

in Partial Fulfilment of the Requirements

for the Degree

Master of Science

McMaster University

Master of Science (2011) McMaster University

(Physics and Astronomy) Hamilton, Ontario

TITLE: SMA Observations of the Local Galaxy Merger Arp 299

AUTHOR: Kazimierz Sliwa, B.Sc. (University of Toronto)

SUPERVISOR: Christine D. Wilson

NUMBER OF PAGES: xi, 90

Abstract

Ultra/Luminous infrared galaxies (U/LIRGs) are some of the most amazing systems in the local universe exhibiting extreme star formation triggered by mergers. Since molecular gas is the fuel for star formation, studying the warm, dense gas associated with star formation is important in understanding the processes and timescales controlling star formation in mergers. We have used high resolution (∼2.3") observations of the local LIRG Arp 299 (D= 44Mpc) to map out the physical properties of the molecular gas. The molecular lines ^{12}CO J=3-2, ^{12}CO J=2-1 and ^{13}CO J=2-1 were observed with the Submillimeter Array and the short spacings of the ^{12}CO J=3-2 and J=2-1 observations have been recovered using James Clerk Maxwell Telescope single dish observations. We use the radiative transfer code RADEX to measure the physical properties such as density and temperature of the different regions in this system. The RADEX solutions of the two galaxy nuclei, IC 694 and NGC 3690, show two gas components: a warm moderately dense gas with $T_{kin} \sim$ 30-500 K (up to 1000 K for NGC 3690) and $n(\mathrm{H_2}) \sim 0.3$ - 3 $\times$ 10^3 cm^{-3} and a cold dense gas with $T_{kin} \sim$ 10-30 K and $n(\mathrm{H_2}) > 3 \times 10^3$ cm^{-3}. The overlap region is shown to have a well-constrained solution with $T_{kin} \sim$ 10-30 K and $n(\mathrm{H_2}) \sim$ 3-30 $\times$ 10^3 cm^{-3}. We estimate the gas masses and star formation rates of each region in order to derive molecular gas depletion times. The depletion time of each region is found to be about 2 orders of magnitude lower than that of normal spiral galaxies. This can be probably explained by a higher fraction of dense gas in Arp 299 than in normal disk galaxies.

To my parents

Acknowledgements

First, I'd like to thank my supervisor Dr. Christine Wilson. She took a chance on me, who knew nothing of the submillimeter world and I'd like to thank her for giving me the opportunity to work with her. Her guidance and patience over the last 2 years helped clear and simplify a lot of things. Without her help this project would not have been this awesome.

I'd also like to thank my committee members Dr. Laura Parker and Dr. Ethan Vishniac for their feedback and comments. I also thank Susanne Aalto for allowing me to use her OVRO CO J=1-0 map of Arp 299 in my research.

I wish to thank the wonderful friends that I made here at McMaster. Our coffee runs, softball games and lunch discussions have been fun. A big thanks to my bro and officemate, Max Schirm and my group mate Tara Parkin who I have had many discussions with about research and for helping me along the way.

Last but not least, I thank my parents who have raised and loved me. This thesis is dedicated to them.

Table of Contents

List of Figures

List of Tables

Chapter 1

Introduction

1.1 U/LIRGs

Ultra/Luminous infrared galaxies (U/LIRGs) are some spectacular objects in the local universe and exhibit extreme star formation. They emit a large portion of their total luminosity at far-infrared wavelengths (LIRGs: $L_{FIR} \sim 10^{11-12}\ L_{\odot}$; ULIRGs: $L_{FIR} > 10^{12}\ L_{\odot}$). Early optical studies have shown that a large fraction of U/LIRGs show morphologies that resemble systems that are interacting or merging (Armus et al., 1987). High resolution optical and near-infrared imaging has revealed that a large fraction of U/LIRGs have nuclear separations of 0.3 - 48 kpc (Murphy et al., 1996). The mergers are likely the origin of the extreme far-infrared luminosities observed. Other systems that appear to be strongly interacting with similar nuclear separations but their far-infrared luminosities do not classify them as U/LIRGs are also observed (eg. NGC 4038/39). These other merging systems raises the question whether all LIRGs go through a ULIRG phase at some point during their merger.

U/LIRGs have been observed to contain a large amount of molecular gas with $M(H_2)$ up to about 10^{10} $M_\odot$ (Sanders et al., 1986). The molecular gas is seen to be concentrated near the nuclear regions within a radius of 0.5 kpc (Sanders & Mirabel, 1996). Subarcsecond resolution CO observations have revealed rotating disks of molecular gas that has been driven to the nuclei (Downes & Solomon, 1998). Theoretical models have shown that during the collision, the gas loses angular momentum due to dynamical friction which causes the gas to decouple from the stars and flow inwards towards the nuclei (Barnes & Hernquist, 1991). The concentrated molecular gas provides fuel for star formation and/or for an active galactic nucleus (AGN).

1.1.1 AGN or Star Formation?

One of the biggest questions regarding U/LIRGs is what powers the extreme infrared luminosities. There are two possible explanations, an AGN or recently formed massive stars. Genzel et al. (1998) tackled this problem by comparing the *ISO* mid-infrared spectroscopy of a sample of 15 ULIRGs to 30 starburst and AGN template galaxies. The [S III] 18.7μm/33.5μm line ratio increases with electron density and is independent of the ionization parameter and the spectral shape of the ultraviolet (UV) radiation field. The extinction corrected [S III] 18.7μm/33.5μm line ratio yields a constant electron density ($n_e \sim 10^{2-2.5}$ cm^{-3}); high to low-excitation ionic lines thus provide a good probe for the hardness (effective temperature) of the ionizing UV radiation field (Genzel et al., 1998). Genzel et al. (1998) found that seven out of ten galaxies (excluding ULIRGs without line detections) have line ratios

([Ne V]/[Ne II] and [O IV]/[Ne II]) indicating a UV radiation field softer than typical AGN radiation fields and are similar to that of starburst galaxies. Definitely one ULIRG (Mrk 231) and perhaps a second (Mrk 273) are seen to have a hard UV radiation field caused by an AGN.

Another indicator of an AGN dominated source is to look at the unidentified emission bands at 3.3, 6.2, 7.7, 8.7 and 11.2 μm which are probably emitted by polycyclic aromatic hydrocarbons (PAHs) or very small amorphous carbon dust grains that are exposed to a moderately intense UV radiation field (Puget & Leger, 1989). Roche et al. (1991) have demonstrated that the PAH features are faint or absent for AGNs and are strong in HII/starburst galaxies. Genzel et al. (1998) find that this trend for PAHs is in good agreement with their sample where the feature at 7.7μm is strong in dusty environments with a moderately strong UV radiation field, such as a starburst and photodissociaton regions (PDRs). Out of the 15 ULIRGs, 12 have similar strength of the 7.7μm feature to the starburst templates. Using this information, they determined the amount that the AGN and massive star formation contribute to the total luminosity using a simple mixing model where an AGN has [O IV]/[Ne II] $\sim$ 1 and PAH strength $\sim$ 0.04 and a starburst has [O IV]/[Ne II] $\sim$ 0.02 and PAH strength $\sim$ 3.6. On average, the ULIRGs have a 5% - 30% contribution from an AGN with 70%-95% coming from star formation. The ULIRGs that are likely dominated by AGNs, Mrk 273 and Mrk 231, may have an AGN contribution of 40% - 80%.

These results show that ULIRGs on average appear to be composite objects with star formation the dominant source of the total infrared luminosity. Gen-

zel et al. (1998) do not find a trend in AGN importance with the stage of the merger. They conclude that at any given stage of the merger, the compression of the circumnuclear gas and the local accretion rate onto the central black hole are what determines whether the star formation or the AGN component dominates the overall energy output.

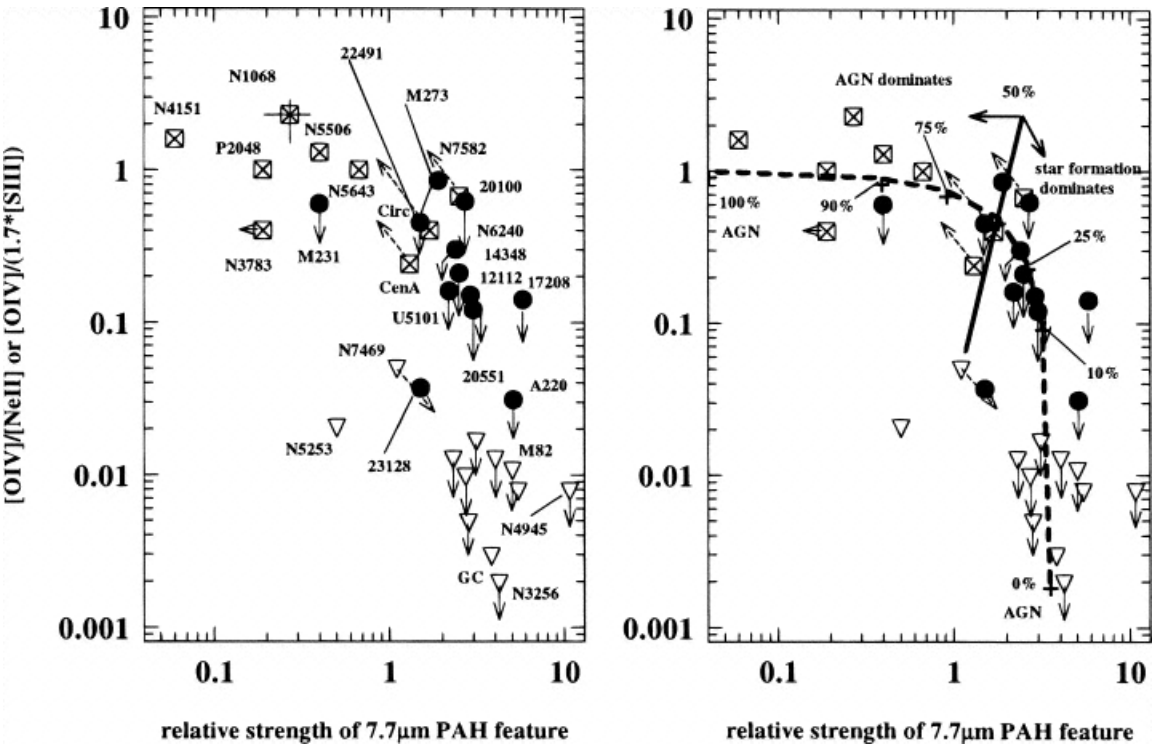

Figure 1.1 Figure 5 from Genzel et al. (1998) showing a new diagnostic diagram combining the extinction corrected 25.9 μm [O IV]/12.8μm [Ne II] line ratio with the relative strength of the 7.7 μm PAH feature for starbursts (*open triangles*), ULIRGs (*filled circles*), and AGNs (*crossed rectangles*). Downward arrows denote upper limits. (*right*): The solid line denotes a simple linear "mixing" curve, made by combining various fractions of the total luminosity in an AGN and a starburst.

1.1.2 L_{IR} vs. L_{HCN}

Solomon et al. (1992) was one of the first to study the dense molecular gas in U/LIRGs. HCN J=1-0 is a good tracer of dense gas since it has a large dipole moment and requires a density of $n(\mathrm{H_2}) \geq 10^4$ cm^{-3} in order to have a significant excitation. They observed HCN J=1-0 and CO J=1-0 using the IRAM 30m telescope for five U/LIRGs, three interacting systems and two gas rich spiral galaxies as controls. On average they found that the ratio of HCN to CO luminosity was 1/6 for ULIRGS, but only 1/80 for normal spiral galaxies. This suggested that a large fraction of the molecular gas in U/LIRGs is in very dense regions similar to star forming cloud cores. They also find that there exists a tighter correlation between far-infrared and the HCN luminosities than between the far-infrared and CO luminosities. Since star formation occurs in dense gas regions and the far-infrared luminosity traces star formation, this result strongly suggests that the main source of the extreme far-infrared luminosity is star formation even though an AGN may exist. The most interesting result from Solomon et al. (1992) is that on average the ratio of far-infrared to HCN luminosity is similar in both U/LIRGs and normal spirals suggesting that the star formation rate per mass of dense gas is independent of infrared luminosity or the state of the interaction.

Gao & Solomon (2004) analyzed the HCN emission from 65 infrared galaxies which included 9 ULIRGs, 22 LIRGs and 34 normal spiral galaxies. With the larger sample size, they also find a tight linear correlation between the far-infrared and HCN luminosities over 3 orders of magnitude (see Figure 1.2). This correlation can be interpreted as the star formation law in terms of dense

molecular gas having a power-law index of 1.0. This is further strong evidence that star formation is the power source in U/LIRGs. They also find that the HCN-CO correlation is tighter than the infrared-CO correlation. This indicates that the star formation rate (related to L_{IR}) depends on the amount of dense molecular gas present and not on the total molecular gas traced by the CO emission.

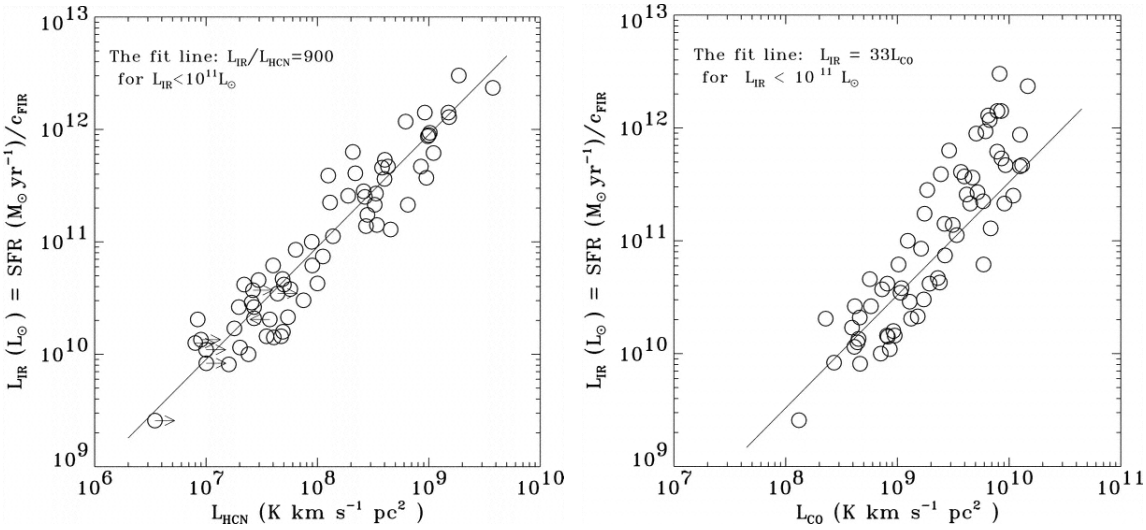

Figure 1.2 Figure 1 from Gao & Solomon (2004) showing (*left*) the L_{IR} versus L_{HCN} correlation in 65 galaxies and (*right*) the L_{IR} versus L_{CO} correlation for the same sample.

1.1.3 Local Analogs to High-z SMGs?

Menéndez-Delmestre et al. (2009) analyzed *Spitzer* mid-infrared spectra of a large sample of submillimeter galaxies (SMGs) and compared them to local ULIRGs. They found that 80% of their sample exhibits PAH features that indicate intense star forming activity just like ULIRGs. Comparing the $S_{7.7\mu m}/S_{11.3\mu m}$ PAH flux ratios shows that SMGs have a radiation environ-

ment similar to that of local starbursts. The distribution of the optical depth determined from the silicate absorption feature at 9.7 μm, $\tau_{9.7\mu m}$, was found to be lower than that seen for local ULIRGs suggesting that the mid-infrared regions of SMGs have a lower dust obscuration. The difference in extinction between ULIRGs and SMGs likely arises from the differences in geometry. The far-infared emission in ULIRGs is seen to be confined in a $\sim$ 1-2 kpc regions (Charmandaris et al., 2002a) while SMGs are seen to have star formation occurring on scales $>$ 2 kpc. Using a composite SMG spectrum, Menéndez-Delmestre et al. (2009) made an estimate of the AGN contribution from the hot dust continuum at $\lambda \geq 10\mu$m. They find that the maximum AGN contribution is $< 32\%$ to the total infrared luminosity, similar to the value found by Genzel et al. (1998). This suggests that the majority of SMGs are also dominated by intense star formation just like local ULIRGs. The differences suggest that ULIRGs are not exact local analogs of high-z SMGs; however, there are enough similarities, that local ULIRGs are often used as templates for SMGs.

1.2 The Target: Arp 299

Arp 299 (NGC 3690 + IC 694, Mrk 171, VV 118, IRAS 11257+5850) is one of the nearest (D = 44 Mpc) examples of a merger system. It has a far-infrared luminosity of $L_{FIR} = 5.5 \times 10^{11}\ L_{\odot}$ (Sanders et al., 2003), classifying it as a LIRG. This system has been studied in great detail in the X-ray (Heckman et al., 1999; Zezas et al., 2003), optical (Jones et al., 1990; Hibbard & Yun, 1999), infrared (Nakagawa et al., 1989; Sugai et al., 1999; Alonso-Herrero et al.,

2000), submillimeter (Sargent & Scoville, 1991; Aalto et al., 1997; Casoli et al., 1999), and radio (Stanford & Wood, 1989; Neff et al., 2004). In the optical, the two nuclei are still distinguishable. Gehrz et al. (1983) showed that there is also a third region of emission thought be associated with the overlap of the two galaxies. This overlap region was once thought to be associated with a third galaxy (Casoli et al., 1989); however, the region shows CO linewidths that are small which is not typical of galactic nuclei (Casoli et al., 1999). High resolution observations show the nuclei are separated by 22″ (4.5 kpc; Sargent et al. 1991). In optical images (see Figure 1.3), there is no obvious evidence of tidal tails but Hibbard & Yun (1999) found two 180 kpc HI tails as well as a faint optical tail displaced from the HI tails. They infer that the merger started 750 Myr ago and the two nuclei will completely merge in roughly 60 Myr. Evolutionary starburst models have shown that Arp 299 has been going through interaction-induced star formation over a span of about 15 Myr (Alonso-Herrero et al., 2000).

1.2.1 X-ray Observations

Some of the first X-ray observations have shown that Arp 299 is one of the most X-ray luminous starburst galaxy in the local universe with an observed luminosity of 4×10^{41} erg s^{-1} in the 0.1-10.0 keV band (Zezas et al., 1998). Recent observations of Arp 299 with the *Chandra Observatory* have detected 18 discrete X-ray sources with luminosities greater than 10^{39} erg s^{-1} (0.5-8.0 keV band) which contributes about 40% of the total galactic emission in this X-ray band (Zezas et al., 2003). Of the 18 discrete X-ray sources, three of

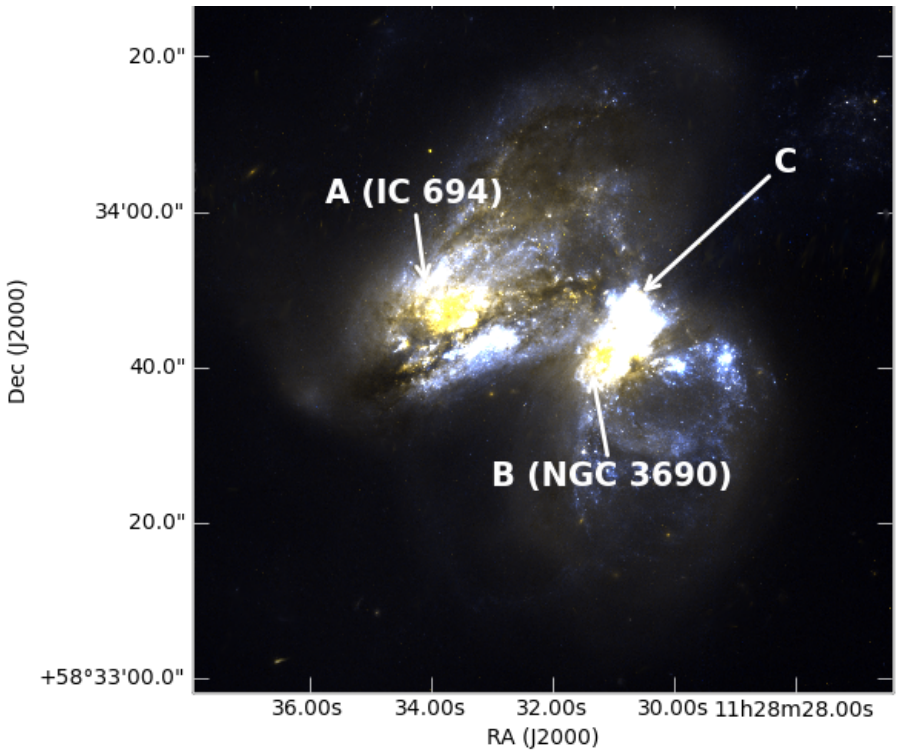

Figure 1.3 *HST* F814W image of Arp 299 with labels denoting the different regions.

them have been identified with the three major regions of star formation (IC 694, NGC 3690 and the overlap region). The source that corresponds to IC 694 (region A) is well fitted by a heavily absorbed (N(H) $\sim 1.2 \times 20^{22}$ cm^{-2}) power law ($\Gamma \sim 1.4$) that is consistent with either a population of X-ray binaries or an AGN.

Heckman et al. (1999) have studied Arp 299 in X-ray and optical. They found that the X-ray spectrum was consistent with that of other starburst galaxies. The X-ray nebula was found to have a luminosity of $\sim 2 \times 10^{41}$ erg s^{-1} and a mass of $\sim 7 \times 10^{9}$ $M_{\odot}$ which can be explained by a collision of the interstellar medium (ISM) of two galaxies (Heckman et al. 1999). Heckman

et al. (1999) suggest another possible origin for the X-ray nebula could be a superwind. The thermal energy content and the dynamical age of the X-ray nebula was found to be consistent with a superwind model and the high mass and X-ray luminosity imply a mass-loaded ($\sim 100\ M_{\odot}$) outflow.

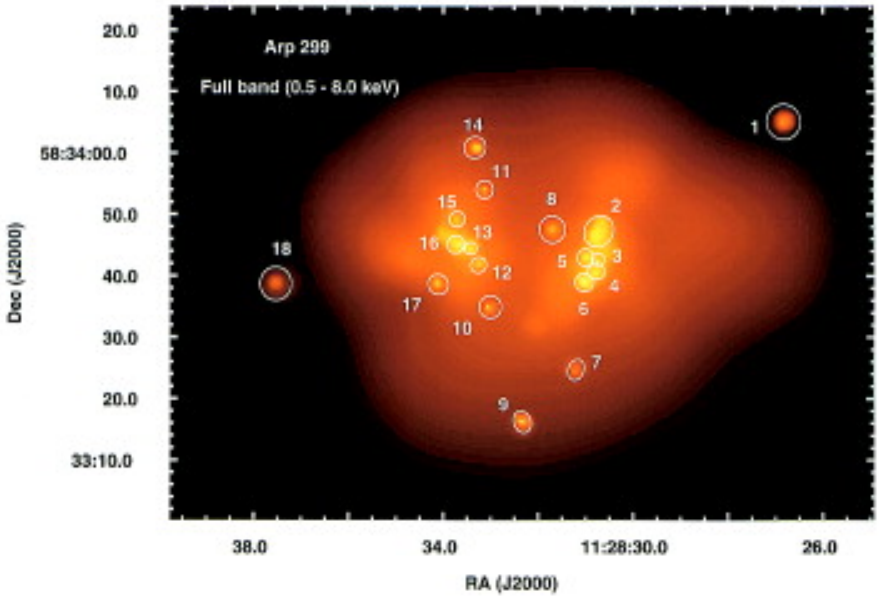

Figure 1.4 Full band (0.5- 8.0 keV) X-ray image of Arp 299 from Zezas et al. (2003). Numbers denote the 18 discrete X-ray sources with luminosities greater than 10^{39} erg s^{-1}.

1.2.2 Near/Mid-Infrared Observations

Hubble Space Telescope NICMOS Paα (see Figure 1.5) images have revealed 19 extremely luminous H II regions equivalent to the luminosity of one of the most active star forming regions in the local Universe, 30 Doradus (the Tarantula nebula; Alonso-Herrero et al., 2000). Finding one or even two of these extremely luminous H II regions is rare in normal galaxies but the chances of finding one in an interacting system is greater (Alonso-Herrero et al., 2000).

Along with the luminous H II regions, 21 older star clusters were found that may have been formed from similar H II regions in the past. Alonso-Herrero et al. (2000) has shown that the overlap region formed massive stars very recently within 4 Myr. They suggest that this region will eventually resemble the appearance of dwarf galaxies.

Spitzer integrated mid-infrared spectra of Arp 299 have been shown to be similar to those of local starbursts (Alonso-Herrero et al., 2009). Only region A, associated with the nuclear region of IC 694, has been shown to have a typical mid-infrared spectrum of a ULIRG that is very compact (<1 kpc) and has dust enshrouded star formation resulting in a deep silicate feature and moderate equivalent widths of the PAHs (Alonso-Herrero et al., 2009). Region A shows no "hot bump" in the range of 3-7μm that is typical of an AGN suggesting that there is no AGN present in region A (Charmandaris et al., 2002b). Region B, the nuclear region of NGC 3690, is seen to have this "hot bump" due to a strong hot-dust component that accounts for 80-90% of the 6μm emission (Alonso-Herrero et al., 2009). This indicates that region B harbors a low-luminosity AGN. *Spitzer* spectral mapping revealed that a large fraction of star formation is occurring in young regions such as the overlap region C and H II regions in the disks of the two galaxies (Alonso-Herrero et al., 2009).

1.2.3 Submillimeter Observations

Interferometric observations of ^{12}CO show strong emission from the three major regions found in infrared images (Sargent & Scoville 1991; Aalto et al.,

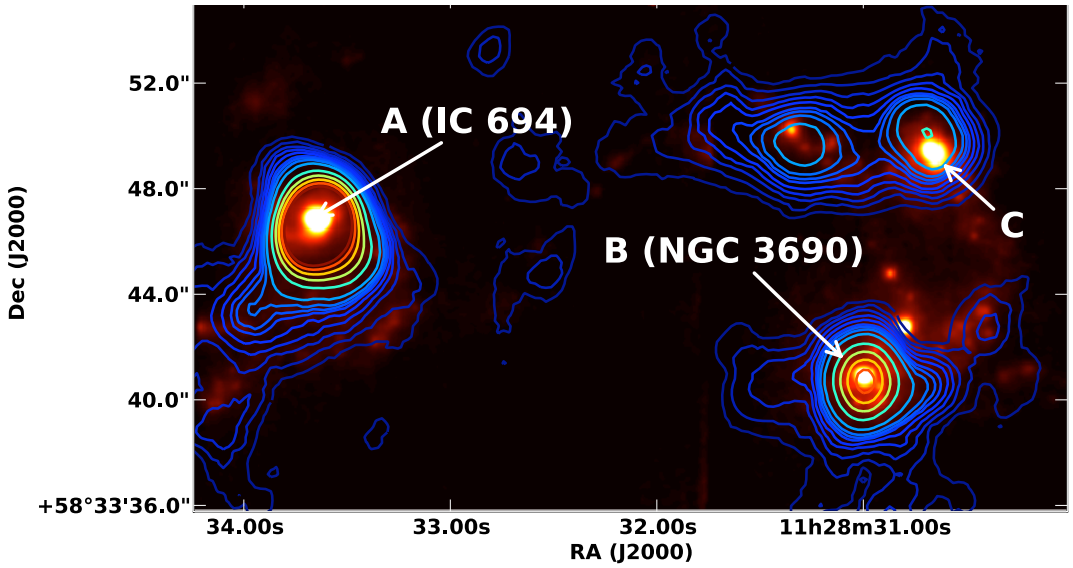

Figure 1.5 NICMOS Paα image of Arp 299 with SMA ^{12}CO J=3-2 contours that correspond to 1, 2..., 9 $\times$ 7.3 Jy/beam km s^{-1}.

1997; Casoli et al., 1999) indicating the presence of large amounts of molecular gas. Sargent & Scoville (1991) estimated a H_2 mass of 3.9 $\times$ 10^9 $M_\odot$ for IC 694 confined within R $\leq$ 250 pc and 0.9 $\times$ 10^9 $M_\odot$ for NGC 3690 confined within R $\approx$ 310 pc. These mass values are most likely overestimates because these masses are over 90% of the dynamical mass (see Section 1.4). Casoli et al. (1999) created a position-velocity cut in their ^{12}CO J=1-0 data cube between region A and B (see Figure 1.6). This cut reveals that there is a gas flow from region A to B. This flow indicates that the regions are physically connected at an early stage of the merger.

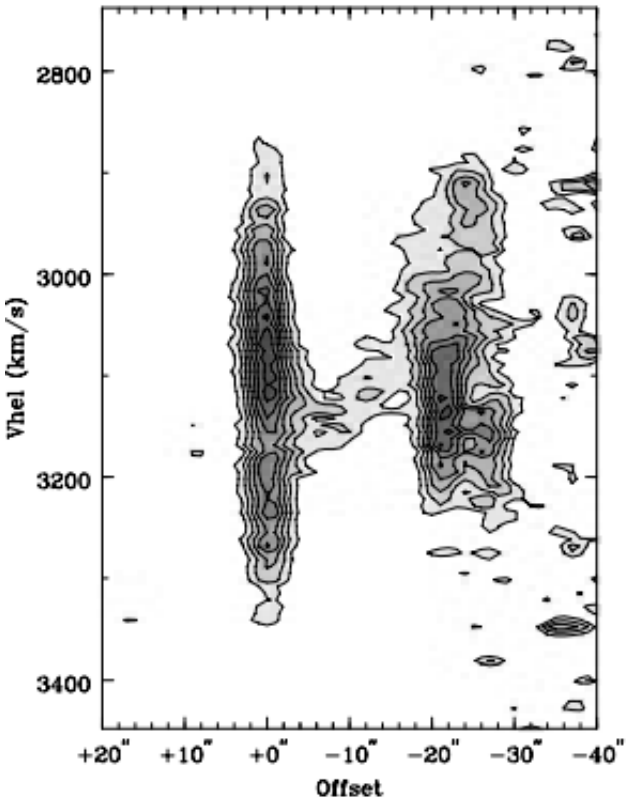

Figure 1.6 Position-velocity cut in the ^{12}CO J=1-0 data cube of Casoli et al. (1999). Region A is set at an offset of 0″ and B at -21.5″

1.2.4 Radio Observations

Pérez-Torres et al. (2010) used the European Very Long Baseline Interferometry Network (EVN) to map IC 694 at 1.7 and 5.0 GHz. Their goal was to characterize the compact sources in the innermost few parsecs region and to detect any recent supernova activity. The EVN observations show that a previously detected source at 5.0 GHz, A1 (see Figure 1.7), has a flat spectrum between 1.7 and 5.0 GHz and is the brightest source at both frequencies. The 1.7 GHz observation shows a diffuse, low-surface brightness emission extending from A1 to another source A5 westwards (see Figure 1.7). This emission

displays a clear core-jet structure which leads to the belief that A1 is the location of the long-sought AGN of IC 694. The complex has a morphology, spectral index, radio luminosity and radio-to-soft X-ray luminosity ratio that resembles a low-luminosity AGN.

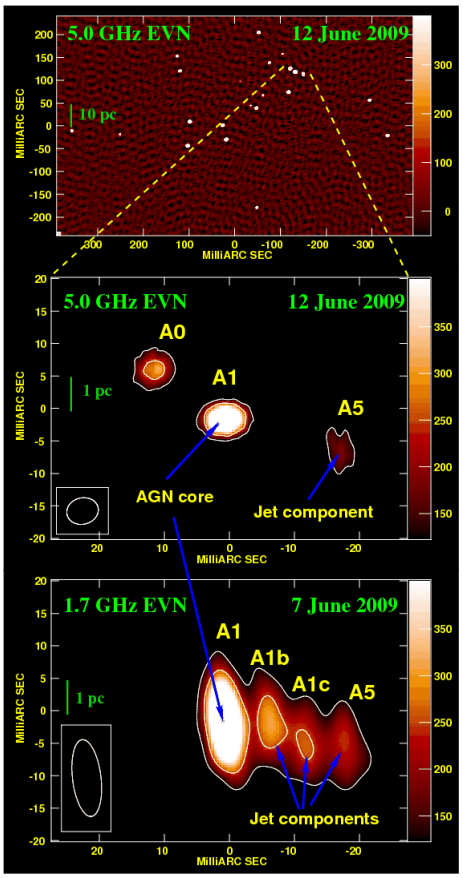

Figure 1.7 EVN observations of IC 694 published in Pérez-Torres et al. (2010).

1.3 Molecular Gas Tracers

Molecular gas is the current and future source of star formation. In our Galaxy and nearby galaxies, most of the star formation occurs in massive, dense ($n(\mathrm{H_2}) \sim 10^{2-5}$ cm^{-3}) and cold ($T \sim$ 10-30 K) giant molecular clouds

(McKee & Ostriker, 2007). Studying the physical conditions and distribution of the warmer (T $\sim$ 30 K), dense gas associated with star formation may help in understanding the processes and timescales controlling the star formation in galaxy mergers. The most abundant molecule in galaxies is molecular hydrogen, H_2. Unfortunately, we cannot detect H_2 easily because it does not have a permanent dipole moment. However, we can detect the next most abundant molecule, carbon monoxide, CO. CO is a very stable molecule that has a weak dipole moment (μ_e =0.11 Debye; Solomon & Vanden Bout 2005). The fundamental transition frequency for CO (J=1-0) of 115.271 GHz is excited by collision with molecular hydrogen even in clouds with low kinetic temperatures tracing gas with temperatures of $\sim$5 K and densities of 100 cm^{-3}. This makes CO the best known tracer for molecular gas. However, the ground state rotational transition of CO is sensitive to all H_2, some of which may not be dense enough to be involved in star formation. The ^{12}CO J=3-2 transition line (ν = 345.796 GHz) probes regions with densities of 2.1 $\times$ 10^4 cm^{-3} and temperatures of 33 K making it a good tracer of the warm, dense gas associated with star formation activity.

1.4 CO Luminosity to H_2 Mass

The H_2 mass to CO luminosity relation is given by

$$M(\mathrm{H_2}) = \alpha L'_{CO} \tag{1.1}$$

where $M(H_2)$ is the total molecular gas mass in $M_\odot$ and L'_{CO} is the CO luminosity in K km s^{-1} pc^2. For our Galaxy, three independent methods result in the same linear relation for the gas mass and the CO luminosity, α = 3.2

$M_\odot$ (K km s^{-1} pc^2)$^{-1}$ (X_{CO} = 2 $\times$ 10^{20} cm^{-2} (K km s^{-1})$^{-1}$; Strong et al. 1988). Early studies of U/LIRGs using this conversion factor found that the gas mass was comparable to or even greater than the dynamical mass inferred by the CO line widths (Scoville et al., 1991). This led to a new model for CO emission from U/LIRGs (Downes et al., 1993; Downes & Solomon, 1998). Molecular clouds in the Galaxy are thought to be virialized (i.e. self gravitating). However, this may not be true for U/LIRGs but the CO emission may come from a filled intercloud medium, in which the linewidth is determined by the total dynamical mass in the region. They find the quantity $\alpha L'_{CO}$ actually measures the geometric mean of the total mass and gas mass. This means that this quantity underestimates the total mass and overestimates the gas mass (see Solomon & Vanden Bout 2005 for a review). Therefore, if CO emission comes from intercloud medium bound by the potential of the galaxy, the constant α has to be modified and is lower than 2.6n$^{1/2}$/T$_b$ where n is the gas density and T$_b$ is the brightness temperature of the gas. Dickman et al. (1986), were the first to assume that α depends on n$^{1/2}$/T$_b$. They suggested that basic uncertainties in density, velocity and geometric structure of extragalactic clouds can lead to mass ambiguities possibly as large as a factor of 3. Even before Downes et al. (1993) and Downes & Solomon (1998), α was thought to differ in starbursts where cloud conditions can vary greatly from clouds in our own Galaxy.

Downes & Solomon (1998) used kinematic models in which most of the CO emission comes from a warm moderately dense intercloud medium to account for the rotation curves, density distribution, size, turbulent velocity and mass of the molecular rings seen in U/LIRGs. Instead of using the standard con-

version factor to determine the gas mass, a radiative transfer model was used and resulted in gas masses of $\sim 5 \times 10^9\ M_\odot$. This gas mass is about four times less than the standard method and leads to a ratio of $M_{gas}/L'_{CO} \approx 0.8\ M_\odot$ (K km s^{-1} pc^2)$^{-1}$. This also resulted in a ratio of gas to dynamical mass $M_{gas}/M_{dyn} \approx 1/6$ and a maximum ratio of gas to total surface density μ/μ_{tot} =1/3. Therefore, in order not to over estimate the gas mass for Arp 299, we adopt the conversion factor $\alpha = 0.8 M_\odot$ (K km s^{-1} pc^2)$^{-1}$.

1.5 Radiative Transfer

The radiative transfer equation can be written as

$$dI_\nu ds = j_\nu - \alpha_\nu I_\nu \tag{1.2}$$

where I_ν is the specific intensity, ds is a distance and j_ν and α_ν are the local emission and extinction coefficients, respectively (see Rybicki & Lightman 1979 for a review). We can define the source function by

$$S_\nu = \frac{j_\nu}{\alpha_\nu}. \tag{1.3}$$

We can rewrite Equation 1.2 into its integral form and introduce the optical depth, $d\tau_\nu = \alpha_\nu ds$

$$I_\nu = I_\nu(0) e^{-\tau_\nu} + \int_0^{\tau_\nu} S_\nu(\tau'_\nu) e^{-(\tau_\nu - \tau'_\nu)}\, d\tau'_\nu \tag{1.4}$$

where I_ν is the emitted radiation from the medium and $I_\nu(0)$ is the background radiation entering the medium.

The above equations are valid for continuum radiation or for spectral lines. Assume that giant molecular clouds have large internal velocities that Doppler

shifting the emission to a different frequency such that, if it does not get reabsorbed locally, it will not be reabsorbed by another region of the cloud. In this case, solving the radiative transfer equations becomes a local problem and we can express the source function as

$$S_{\nu_{ul}} = \frac{2h\nu_{ul}^3}{c^2}\left(\frac{g_u n_l}{g_l n_u} - 1\right)^{-1} \tag{1.5}$$

where n_i is the number density of molecules in the i^{th} energy state and g_i is the statistical weight of energy state i. The optical depth for a homogenous medium can be expressed as

$$\tau = \frac{c^3}{8\pi\nu_{ul}^3}\frac{A_{ul}N_{mol}}{1.064\Delta V}\left[x_l\frac{g_u}{g_l} - x_u\right] \tag{1.6}$$

where A_{ul} is the Einstein coefficient for spontaneous emission, N_{mol} is the molecular column density, ΔV is the full width half-maximum (FWHM) in velocity units and x_i is the fraction population of level i. A radiative transfer code solves for the relative populations of the energy states of the molecule which allows for the calculation of the optical depth (van der Tak et al., 2007). The radiative transfer model supplies us with the flux of molecular lines at a certain kinetic temperature (T_{kin}), density ($n(\mathrm{H_2})$) and molecular column density (e.g. $N(^{12}\mathrm{CO})$). We can use line ratios to eliminate the problem of the unknown constant, the beam filling factor, if we assume that the same regions are emitting the observed radiation in the beam. We can constrain the physical conditions by determining where the line ratios have the same kinetic temperature and density.

1.6 Interferometry vs. Single Dish

The resolution of a single dish telescope is limited by the size of the dish (resolution $\propto \lambda/\mathrm{D}$). The bigger the dish, the better resolution that can be achieved. However, building huge dishes is not very practical and would be very expensive. Instead, we can use our knowledge of light and synthesize a large aperture by using an array of small dishes. Interferometry uses a number of dishes spread apart to create a map that is equivalent to what a large dish would observe. Since the resolution depends on the distance between pairs of dishes, the further the separation, the better the resolution. This, however, comes at a price. Since we cannot get two dishes to have zero separation between them, we have missing short spacings in the uv-plane (see Figure 1.8). The uv-plane is the projections of the baselines (i.e. physical separation of a pair of dishes) in the Fourier plane. As the Earth rotates, each pair traces out a curve of data points that fills in the uv-plane. The uv-plane can be Fourier transformed into the image plane. Since short baselines Fourier transform into large scale features, the missing short spacings indicate that we are missing these large scale features; therefore, we are missing flux.

The CLEAN task, the task that produces the clean image for science analysis, attempts to extrapolate the missing short spacings but for most cases fails to recover them. The best way to recover the missing flux is to observe the source with a single dish telescope. The points on the single dish can be treated as single "elements" and pairs of elements can give us a baseline; therefore we can Fourier transform the single dish observations into the uv-plane. We can then combine the single dish and interferometric observations together to get a complete map. To choose a good single dish observatory to comple-

ment the interferometric observatory requires that the single dish diameter be at least double the size of a dish in the interferometric observatory. This is to ensure that we can get an overlap in the *uv* data in order to calculate an appropriate scaling factor in calibration. An example is the Plateau de Bure (PdB) interferometric observatory which consists of six 15 m dishes. In order to complement the array and to recover the short spacings, the IRAM 30 m single dish observatory is used.

1.7 The Goal

Since molecular gas is required for current and future star formation, studying the physical properties and distribution of the warm, dense gas is important in understanding the processes and timescales that control the star formation in galaxy mergers. In this thesis, we re-analyze the Submillimeter Array observations of ^{12}CO and ^{13}CO of Arp 299 published in Wilson et al. (2008). We constrain the physical conditions such as temperature and density by combining the molecular-line observations with radiative transfer models obtained using the radiative transfer code RADEX. In Chapter 2, we describe the observations and creation of the line ratio maps. In Chapter 3, we present our findings from our radiative transfer models for each region and other properties such as gas and dynamical masses from the SMA maps. In Chapter 4 we discuss our findings from Chapter 3.

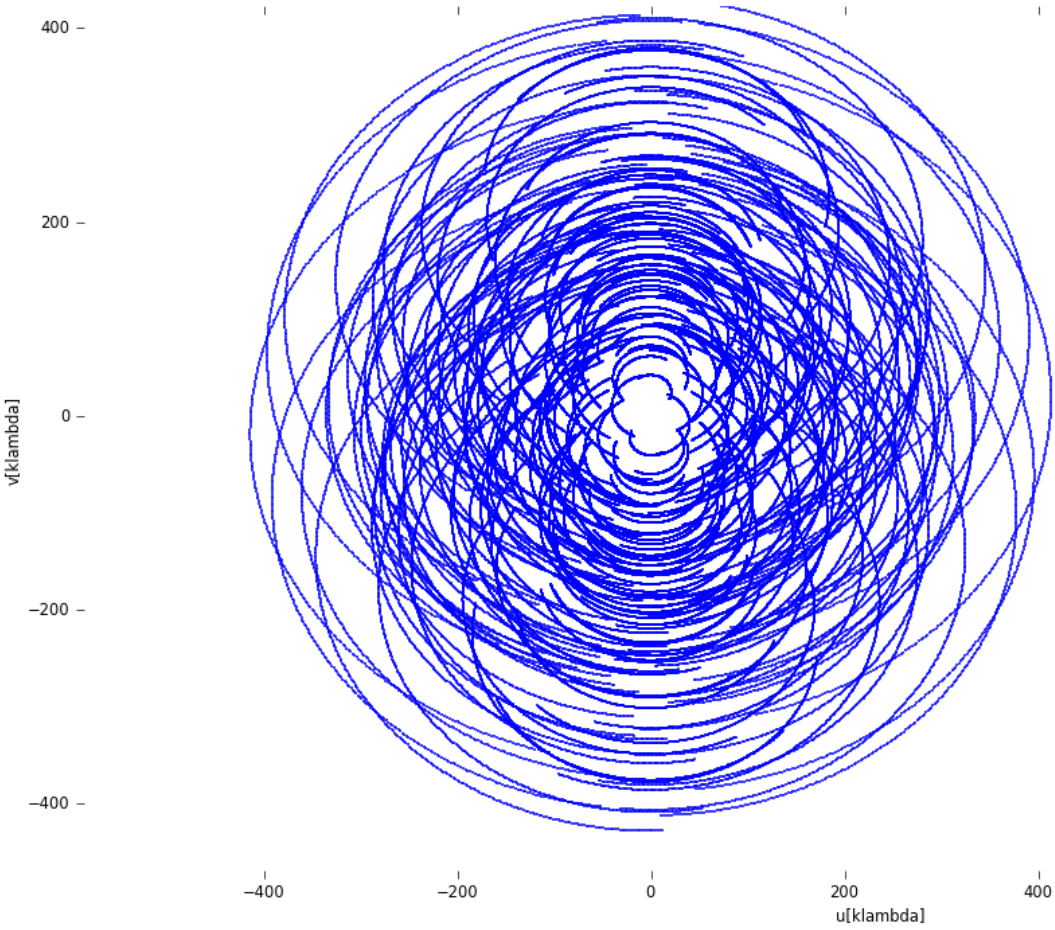

Figure 1.8 *uv*-plane for a 10 hour simulated ALMA observation of a source at Dec=-58° using CASA in the extended configuration for the early science phase. The missing coverage in the middle indicates that we are missing large scale structures.

Chapter 2

Observations/Reduction

2.1 Submillimeter Array

Arp 299 was observed with the Submillimeter Array (SMA;Ho et al. 2004) on 2006 April 10 for the ^{12}CO J=3-2 transition line and 2007 March 27 for the CO J=2-1 transition line. The data was first published in Wilson et al. (2008). The correlator was configured to have a spectral resolution of 0.8125 MHz corresponding to roughly 1.1 km s^{-1} for CO J=2-1 and about 0.7 km s^{-1} for CO J=3-2 (Wilson et al., 2008). A bandwidth of 2 GHz was chosen, which covers 24 chunks overlapping slightly in frequency in each of the lower and upper sidebands. The ^{12}CO J=2-1 was centered in the upper sideband and the ^{13}CO J=2-1 was observed simultaneously in the lower sideband 10 GHz away. The ^{12}CO J=3-2 was observed in the lower sideband and the HCO+ J=4-3 transition line was observed in the upper sideband. We do not make use of the HCO+ J=4-3 since for Arp 299, only half of the line was observed. The SMA was set in the compact array configuration corresponding to unprojected

baselines of 16-69m. The largest scale feature to which our data are sensitive is given by

$$\text{Resolution(arcsec)} = 206264.8\frac{\lambda}{D} \tag{2.1}$$

where D is the baseline length. Using the shortest unprojected baseline (16m) we get 17″ (3.6 kpc) for CO J=2-1 and 12″ (2.6 kpc) for CO J=3-2. The SMA has a field of view of ∼55″ for CO J=2-1 and ∼36″ for CO J=3-2. Since Arp 299 has sufficiently extended emission, a small mosaic of two pointings was used (see Figure 2.1). For the CO J=2-1 observations, all eight antennas were used and the total on-source integration time was 6.6 hours and for the CO J=3-2, only seven antennas were used and the total on-source integration time was 5.6 hours.

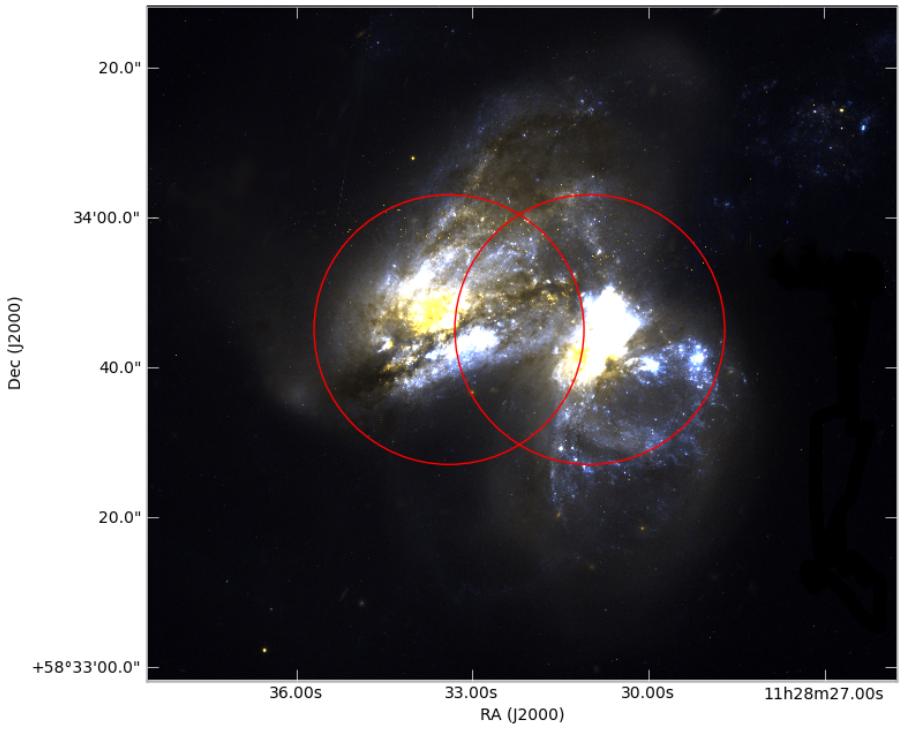

Figure 2.1 HST image of Arp 299 with the SMA ^{12}CO J=3-2 overlapping field of views in the mosaic.

The initial calibration was done using the MIR software package (refer to Wilson et al., 2008 for more details). After the calibration, the data were exported into MIRIAD (Sault et al., 1995) format for further editing and imaging. However, with the release of the new reduction package for the next generation observatories, CASA, we opt to edit and image the data in CASA instead of MIRIAD. The *uv* data was exported into FITS format and then imported into CASA format. The data was first flagged to remove the first six and last six channels of each of the 24 chunks of the correlator. The data was also flagged to remove high-amplitude value data points (> 100 for CO J=3-2; > 60 for CO J=2-1). This removes less than 1% of the data that may introduce artifacts into our maps. The continuum emission was subtracted in the *uv*-plane using the line-free channels before imaging. This was extremely important for the ^{13}CO J=2-1 data set because the continuum was up to 70% of the total emission.

The data sets were inverted and cleaned using the CASA task *clean* using a robust weighting scheme in order to achieve a good balance between sensitivity and resolution. Data cubes of 20 km s^{-1} and 50 km s^{-1} velocity resolutions were made for each data set. Each data set was cleaned down to 2 times the rms noise in each velocity channel. The beam (see Figure 2.2) looks sufficiently clean and the emission looks sufficiently compact that cleaning in the inner quarter region of the image produces good results. However, for the ^{12}CO J=2-1 and J=3-2 data sets clean boxes were added around regions with known emission from Arp 299 in each channel interactively. This was not possible for the ^{13}CO J=2-1 data set because the emission is weak; therefore the entire inner quarter region was cleaned. The data cubes were corrected

for the primary beam pattern which is important for mosaic images. Finally, integrated intensity (moment 0) maps were created using pixels with values greater than 2σ and channels that clearly contain emission from Arp 299 (see Figures 2.3 - 2.5). Spectra of each region of emission are presented in Figure 2.6.

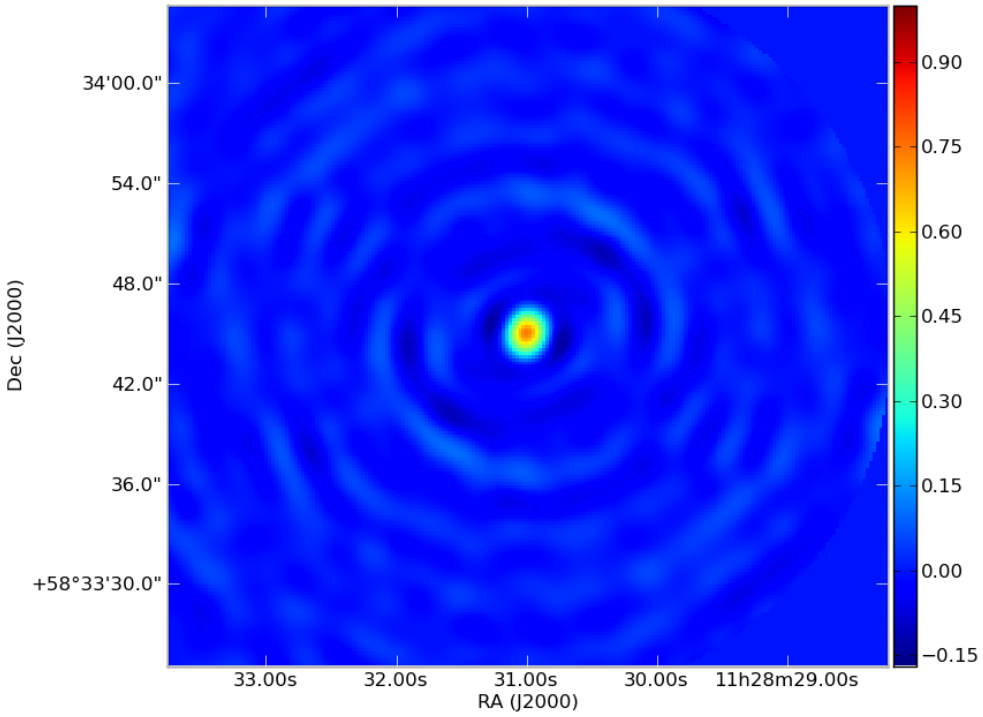

Figure 2.2 The synthesized dirty beam of the SMA ^{12}CO J=3-2 observations.

2.2 ^{12}CO J=1-0 Map

We have obtained the ^{12}CO J=1-0 data cube published in Aalto et al. (1997) with resolution of $2.5'' \times 2.2''$. The data cube was obtained already cleaned and for observation details refer to Aalto et al. (1997). We created an integrated intensity map with a 2σ cutoff (see Figure 2.7). This map will

Table 2.1. SMA Observations Summary

CO Transition Line	Flux (Jy km s^{-1})	Beam ($''$)	rms (mJy/beam)[a]
^{12}CO J=1-0[b]	377± 9	2.5 × 2.2	8.5
^{12}CO J=2-1	1870 ± 29	3.0 × 1.8	16.9
^{13}CO J=2-1	40 ± 2	3.2 × 1.8	10
^{12}CO J=3-2	2818 ± 35	2.2 × 1.9	33

[a]rms values for 20 km s^{-1} channel widths; 50 km s^{-1} channel width for ^{13}CO J=2-1

[b]Map obtained from Aalto et al. (1997); observed with Owens Valley Radio Observatory.

help us add another line ratio in order to better constrain the density and temperature of each region.

2.3 James Clerk Maxwell Telescope

Arp 299 was also observed with the James Clerk Maxwell Telescope (JCMT) on 2007 March 31 for ^{12}CO J=3-2 and 2011 March 09 for ^{12}CO J=2-1. The JCMT was used to make a $2'$ Nyquist-sampled map with the array receiver HARP-B in the CO J=3-2 line resulting in a $15''$ beam and to make a basketweave raster map with the RxA receiver in the CO J=2-1 line resulting in a $22''$ beam. The raw data was made into a cube that spanned from -400 km s^{-1} to 400 km s^{-1} using the *Starlink* software (Currie et al., 2008) written for JCMT data. The cube was then baseline corrected (i.e. continuum subtracted) using line free channels and assuming a first order baseline. Several

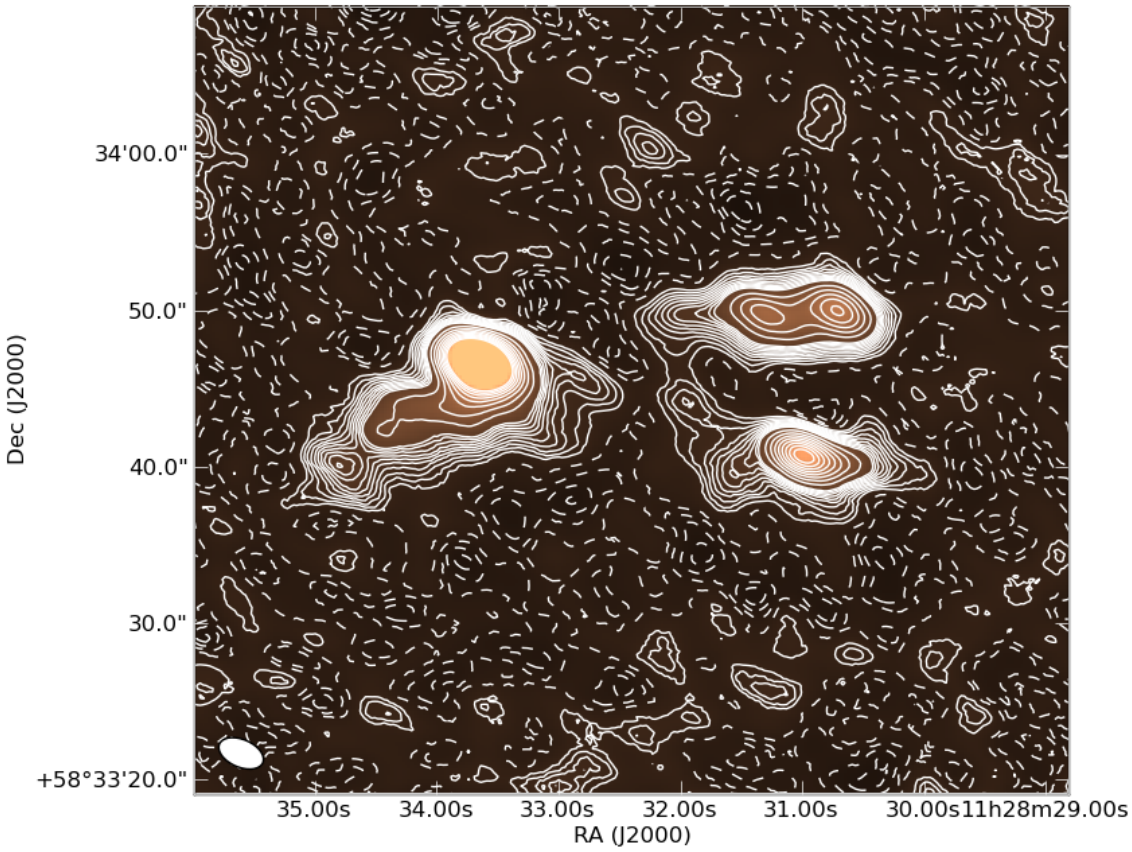

Figure 2.3 SMA ^{12}CO J=2-1 integrated intensity map. Contours correspond to -4, -3, -2, -1, 1, 2..., 10, 15, 20, 25, 30, 35, 40, 45, 50 × 3.4 Jy/beam km s^{-1}. Dashed contours indicate negative flux.

of the outer bad pixels were trimmed off and the cube velocity resolution was degraded to 20 km s^{-1} (see Figure 2.9).

2.4 Morphology

Our interferometric observations of Arp 299 in ^{12}CO J=3-2 and ^{13}CO J=2-1 are the first of its kind. Previous CO interferometric observations include ^{12}CO J=1-0 (Sargent & Scoville, 1991; Aalto et al., 1997; Casoli et al., 1999),

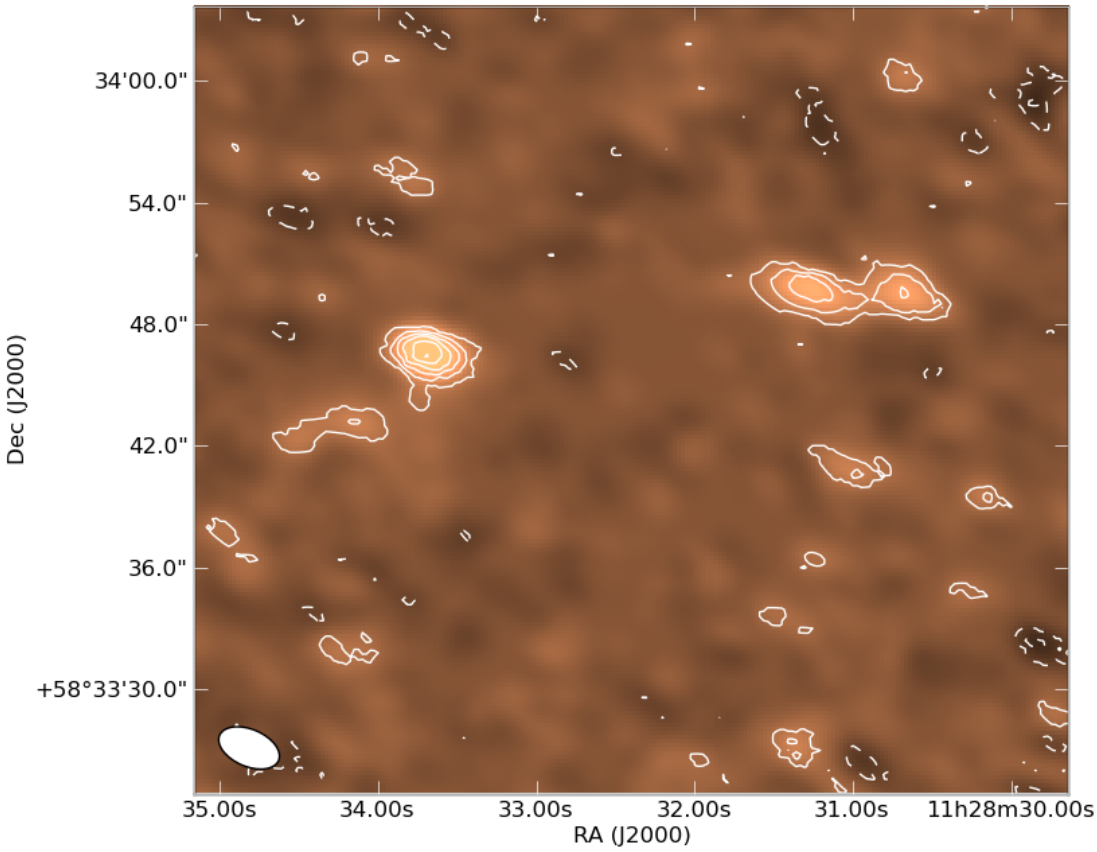

Figure 2.4 SMA ^{13}CO J=2-1 integrated intensity map. Contours correspond to -2, -1, 1, 2..., 10, 15 $\times$ 2.7 Jy/beam km s^{-1}. Dashed contours indicate negative flux.

J=2-1 (Casoli et al., 1999) and ^{13}CO J=1-0 (Aalto et al., 1997; Casoli et al., 1999). We detect the three compact regions of emission in ^{12}CO as in previous observations. To avoid confusion, we adopt the notation of Gehrz et al. (1983), where the source corresponding to IC 694 (eastern source; east is left in our maps) is denoted by A, the source corresponding to NGC 3690 (south west) is denoted by B and the emission corresponding to the overlap region (north west) is denoted by C (see Figure 1.5).

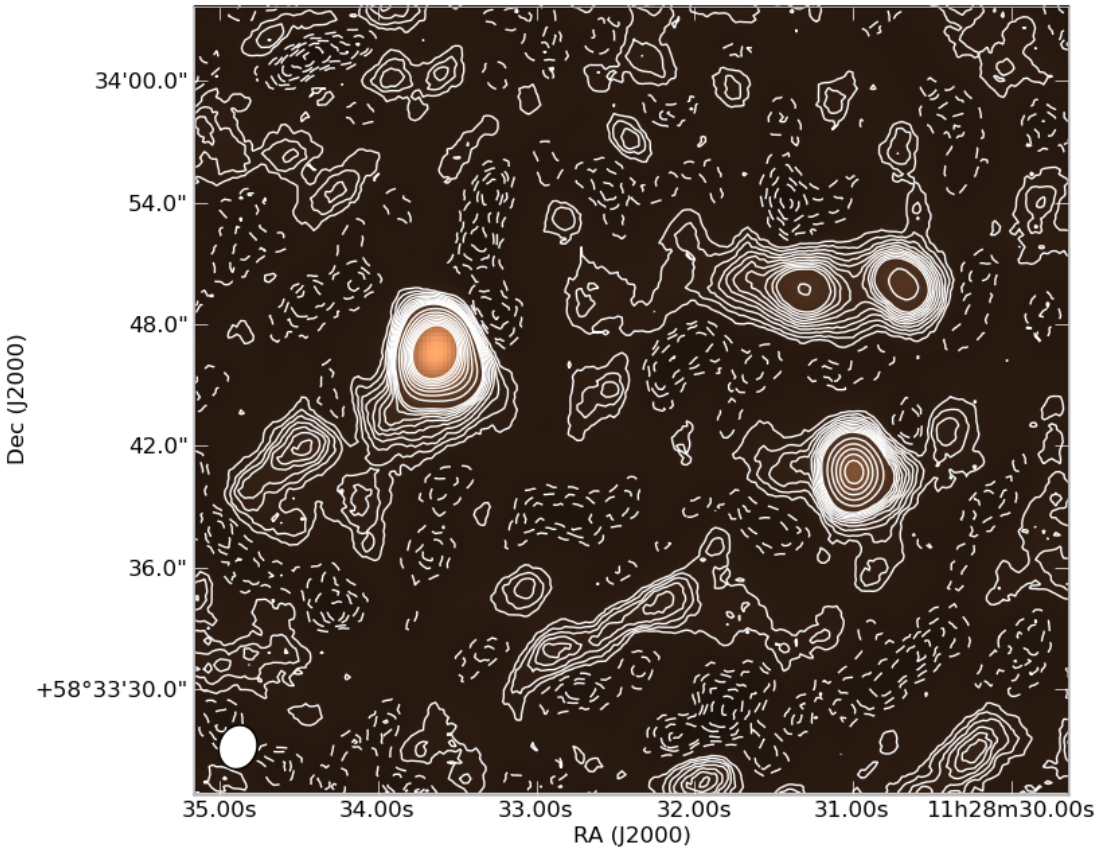

Figure 2.5 SMA ^{12}CO J=3-2 integrated intensity map. Contours correspond to -6, -5, -4, -3, -2, -1, 1, 2..., 10, 15, 20, 25, 30, 35, 40, 45, 50 $\times$ 7.3 Jy/beam km s^{-1}. Dashed contours indicate negative flux.

The interesting case is with the ^{13}CO J=2-1 map. We have good detections for regions A and C but a very weak detection for region B. This is similar to what is seen with the ^{13}CO J=1-0 maps of Aalto et al. (1997) and Casoli et al. (1999). Aalto et al. (1997) has a non detection in the ^{13}CO map at the peak position for region B found in the ^{12}CO map while Casoli et al. (1999) has a weak detection. Casoli et al. (1999) argues that the difference between the Aalto et al. (1997) map and their own can be attributed to different ways of continuum subtraction. Casoli et al. (1999) even obtained a second set

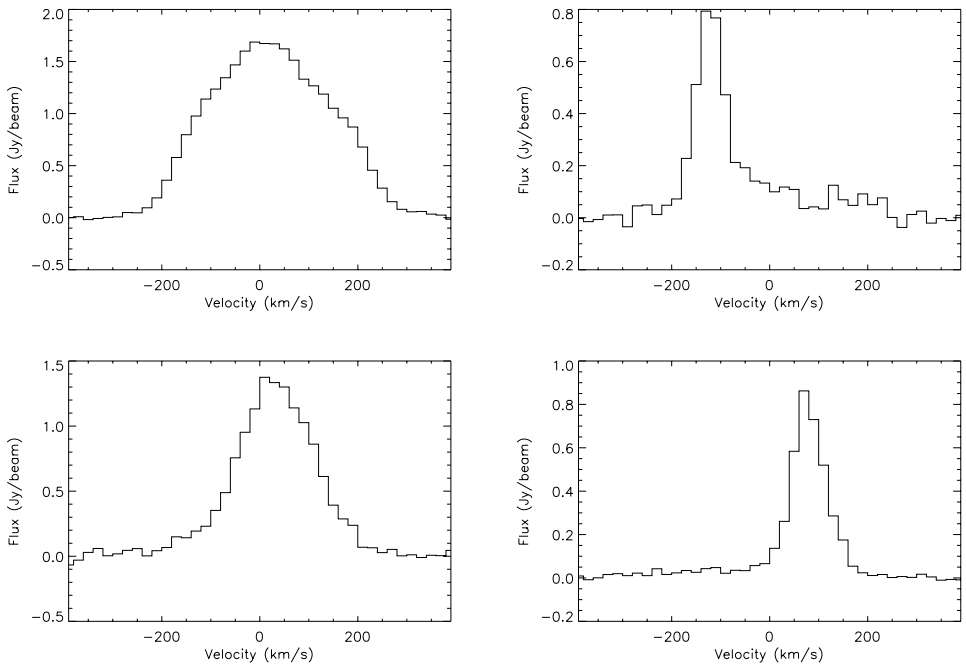

Figure 2.6 SMA ^{12}CO J=3-2 spectra of each region of CO emission: (*top left*) Region A (IC 694), (*top right*) Region A′ (IC 694 disk), (*bottom left*) Region B (NGC 3690), (*bottom right*) Region C (overlap)

of observations for ^{13}CO J=1-0 with a lower signal to noise ratio (SNR) and they find the same structure as with their map before. We find that changing the weighting scheme implemented during the creation of the image changes the structure seen. Using a robust weighting (i.e. combination of uniform and natural weighting) that is more uniform (i.e. robust $\leq$0.0) than natural weighting results in a map with a non-detection in region B. This is reasonable since a natural weighting produces the optimal SNR map but poor resolution; therefore we use robust=0.5 whch produces a map with the best compromise between resolution and sensitivity with a detection for region B.

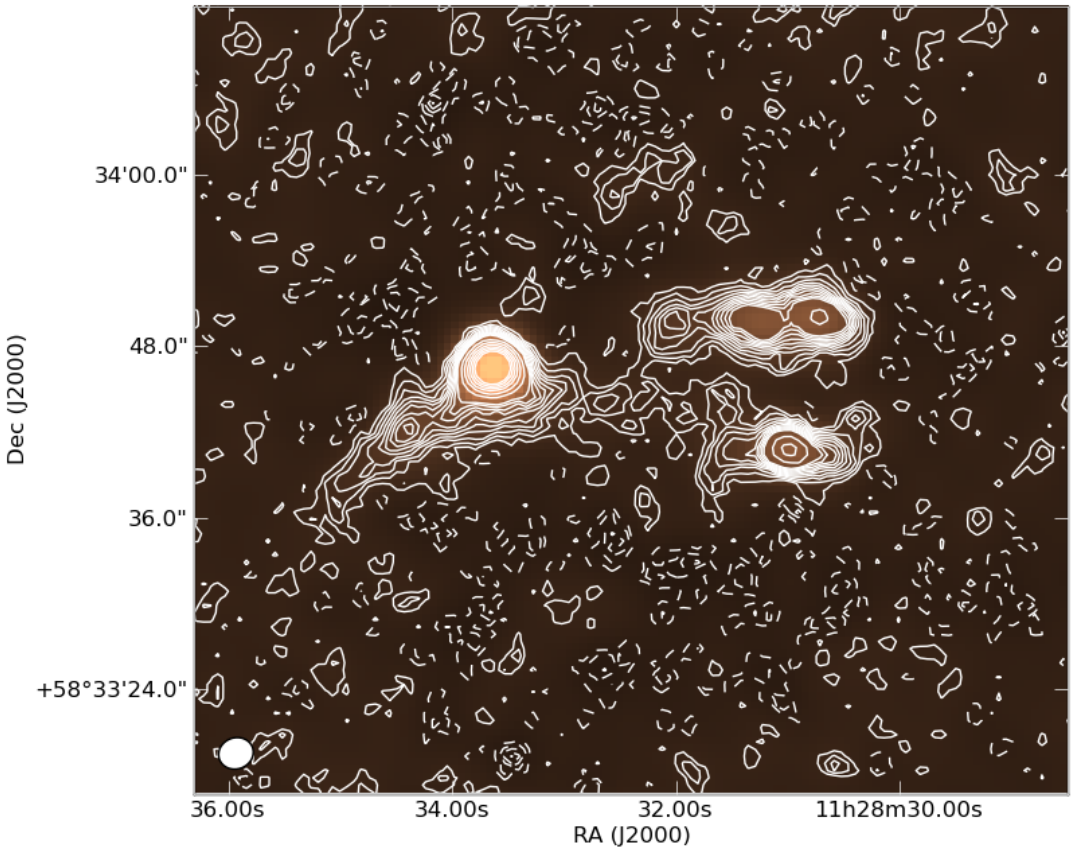

Figure 2.7 Owens Valley Radio Observatory ^{12}CO J=1-0 integrated intensity map from Aalto et al. (1997). Contours correspond to -3, -2, -1, 1, 2..., 10, 15, 20, 25, 30, 35, 40, 45, 50 $\times$ 1.3 Jy/beam km s^{-1}. Dashed contours indicate negative flux.

Casoli et al. (1992) studied six merger systems that included 5 U/LIRGs and found that the ^{13}CO lines are much weaker in these systems than in normal spiral galaxies. They suggest that the weak ^{13}CO emission is not due to peculiar excitation conditions but instead due to an unusually large [^{12}CO]/[^{13}CO] abundance ratio and offer three scenarios that can lead to this effect. One scenario is the ^{13}CO molecules are photo-dissociated efficiently by the strong UV radiation field created by the large number of massive stars while

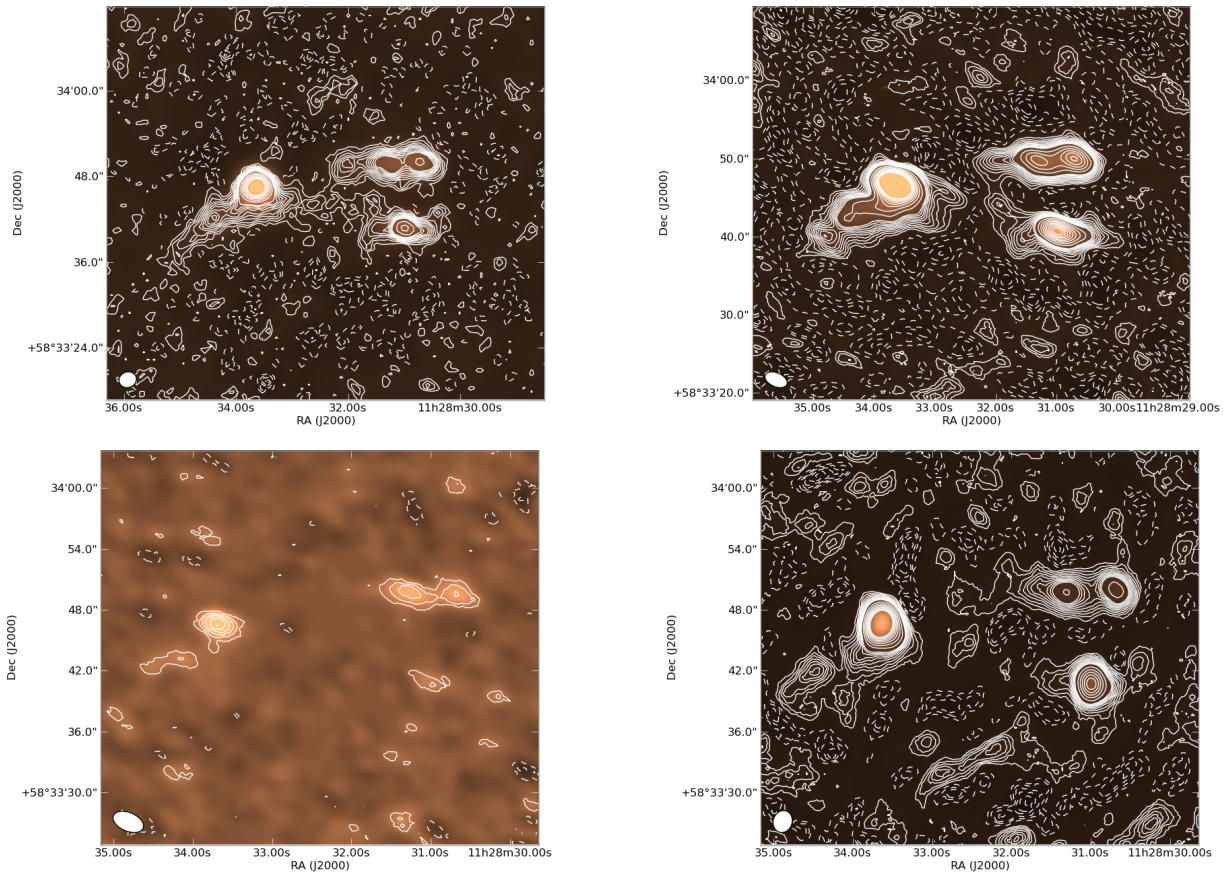

Figure 2.8 SMA integrated intensity maps: (*top left*) ^{12}CO J=1-0; (*top right*) ^{12}CO J=2-1; (*bottom left*) ^{13}CO J=2-1; (*bottom right*) ^{12}CO J=3-2

the ^{12}CO molecules are shielded against this field. This scenario is unlikely because the C^{18}O molecule is even more easily photo-dissociated than the ^{13}CO molecule but the ^{13}CO J= 1-0/C^{18}O line ratio is found to be normal (Casoli et al. 1992). Another scenario is where ^{12}C is replenished in the ISM and thus in ^{12}CO by nucleosynthesis in massive stars formed during the starburst. When the massive stars go supernova they enrich the ISM in ^{12}C while ^{13}C is synthesized in the envelopes of low mass stars in the red giant phase (Vigroux et al. 1976) and is not replenished in the ISM by the end of the starburst. The

last possible scenario could be that atomic gas infall from the outer regions is converted from the atomic to molecular state. This would add large amounts of ^{13}CO poor material to the ISM. Casoli et al. (1992) suggest the last two scenarios are most likely to enhance the [^{12}CO]/[^{13}CO] abundance ratio which could contribute to the weak ^{13}CO detections.

2.5 Short Spacing Flux Correction

In order to recover the short spacings of the ^{12}CO SMA maps, we combine them with the low resolution JCMT maps. The simplest way of achieving this is to use a technique called feathering, which combines the two maps starting in the image plane. The JCMT maps are intrinsically in units of the antenna temperature, T_A^* (K). These units are not very useful for extended sources, so we convert the units to main beam temperature, T_{mb}, since the extended emission likely fills the JCMT beam, using

$$T_{mb} = \frac{T_A^*}{\eta_{mb}} \tag{2.2}$$

where η_{mb} is the main beam efficiency taken from the JCMT website[1] ($\eta_{mb} = 0.6$ for $\nu = 345$GHz and $\eta_{mb} = 0.69$ for $\nu = 230$GHz). Finally the main beam temperature units was converted to Jy/beam to match the SMA units using

$$\frac{\text{Jy/beam}}{\text{K}} = \frac{2.786 \times 10^7}{\pi R_d^2 \times \eta_{mb}} \tag{2.3}$$

where R_d is the radius of the dish in cm. Both maps were binned to the same velocity resolution so that each velocity channel matches in each map. The feathering technique takes both maps, regrids the low resolution image

[1] http://www.jach.hawaii.edu/JCMT/spectral_line/Standards/eff_web.html

to match the high resolution image, Fourier transforms them to the gridded *uv*-plane, sums up the gridded visibilities and then Fourier transforms the feathered map back into the image plane. See Appendix A for a complete script on how to feather two images.

The feathered images of ^{12}CO J=2-1 and J=3-2 are presented in Figure 2.10. Comparing the SMA only maps with the JCMT maps, the ^{12}CO J=2-1 map was missing about 20% of the total flux and the ^{12}CO J=3-2 map was missing about 67% of the total flux (see Table 2.2). The amount of missing flux for the ^{12}CO J=3-2 map found in Wilson et al. (2008) is less than what we find here because Wilson et al. (2008) did not convert T_A^* to T_{mb}, assuming instead that Arp 299 is a point like source in the JCMT beam. We see that the feathering technique has recovered all of the missing flux in the ^{12}CO J=2-1 map while only recovering 77% of the missing flux in the ^{12}CO J=3-2 map. This partial flux recovery in the ^{12}CO J=3-2 may be due to the feather task having determined a scaling factor between the SMA and JCMT maps that is not correct. Comparing the SMA only integrated maps with the feathered integrated intensity maps, we see that the emission in the ^{12}CO J=2-1 map is slightly increased around the three regions of emission, while the ^{12}CO J=3-2 has regions of increased emission to the north east of region A and in between region A and C. From their spectra the increased emission to the north east of region A seem to be artifacts while the increased emission in between region A and C seem real (see Figure 2.11). A possible explanation for the artifacts we see north east of IC 694 is the primary beam correction. When we corrected for the primary beam, the noise in the map is no longer uniform. If the gain in the outer regions of the map is 0.5 and we divide by the gain, the noise is

Table 2.2. SMA versus Feathered Maps

Transition (^{12}CO)	Flux (Jy km s^{-1}) SMA	Feather	JCMT	Missing[a] (%)	Recovered[b] (%)
J=2-1	1870 ± 29	2382 ± 29	2324 ± 430	20	100
J=3-2	2818 ± 35	6577 ±36	8574 ± 600	67	77

[a]Missing flux in the SMA only map relative to the JCMT map.

[b]Recovered flux in the feathered map relative to the JCMT map

increased by 2. Since the integrated intensity maps are created using a single cutoff value, the enhanced noise is not masked out.

2.6 Line Ratio Maps

To create line ratio maps, we need CO maps with the same spatial resolution in order to probe regions on the same spatial scales. The resolution to which we can degrade the maps is limited by the ^{12}CO J=1-0 and the ^{13}CO J=2-1 maps. Therefore, we degrade the resolution of all of our maps to a compromise value of $3.6'' \times 2.4''$ (beam position angle= 66°). The resolution of our SMA CO maps is degraded by applying a gaussian taper weighting to the *uv* data sets. The taper function puts more weight to short baseline data points in order to degrade the resolution. The gaussian taper functions that were applied to each map are presented in Table 2.3. The ^{12}CO J=1-0 map

Table 2.3. Taper Weights

CO Map	Gaussian Taper	Beam PA
^{12}CO J=1-0[a]	$2.76'' \times 0.587''$	60.81°
^{12}CO J=2-1	$1.84'' \times 1.34''$	74.00°
^{13}CO J=2-1	$1.28'' \times 1.187''$	25.90°
^{12}CO J=3-2	$3.618'' \times 0.95''$	69.80°

[a]Gaussian kernel used to smooth the map.

that we obtained was just a clean data cube; therefore, in order to degrade the resolution we applied a gaussian kernel.

The integrated intensity maps were created using pixels with values greater than 2σ and have units of Jy/beam km s^{-1}. We converted the units of the CO maps to K km s^{-1} using the equation

$$S_\nu = \frac{2\nu^2 kT}{c^2}\Omega_B \tag{2.4}$$

where T is the brightness temperature corresponding to flux S_ν and Ω_B is the synthesized beam solid angle. Equation 2.4 can be simplified into the equation

$$(\frac{T}{1K}) = (\frac{S_\nu}{1\text{Jy/beam}})[13.6(\frac{300\text{GHz}}{\nu})^2(\frac{1''}{\theta_{major}})(\frac{1''}{\theta_{minor}})] \tag{2.5}$$

where θ_{major} and θ_{minor} are the synthesized beam major and minor axes. Finally, we created ^{12}CO $\frac{J=3-2}{J=2-1}$, ^{12}CO $\frac{J=2-1}{J=1-0}$ and $\frac{^{12}\text{CO}}{^{13}\text{CO}}$ J=2-1 line ratio maps (see Figures 2.12) by dividing the appropriate maps with a cutoff at 2σ for each map.

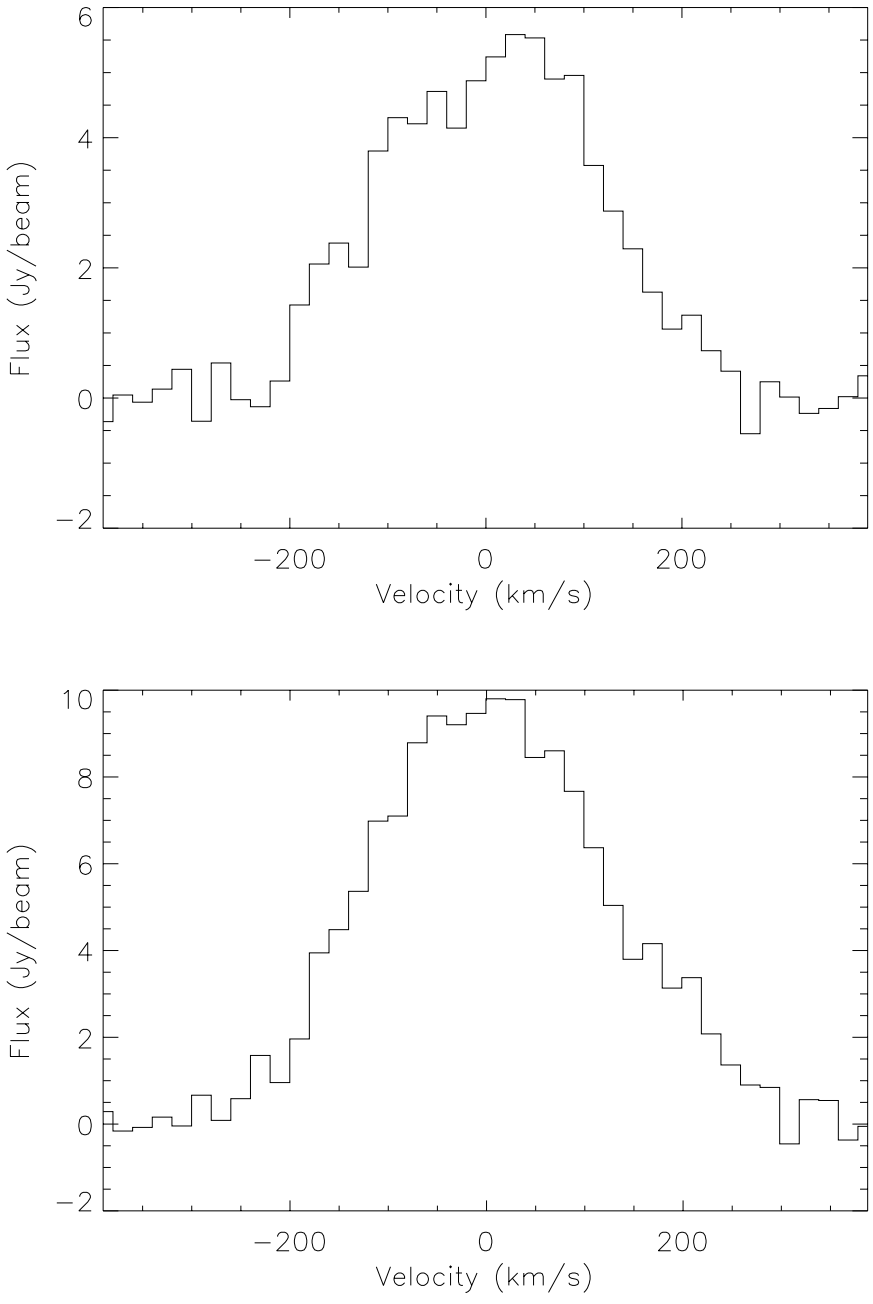

Figure 2.9 JCMT spectra: (*top*): Spectrum at the brightest pixel of the ^{12}CO J=2-1 map; (*bottom*): Spectrum at the brightest pixel of the ^{12}CO J=3-2 map

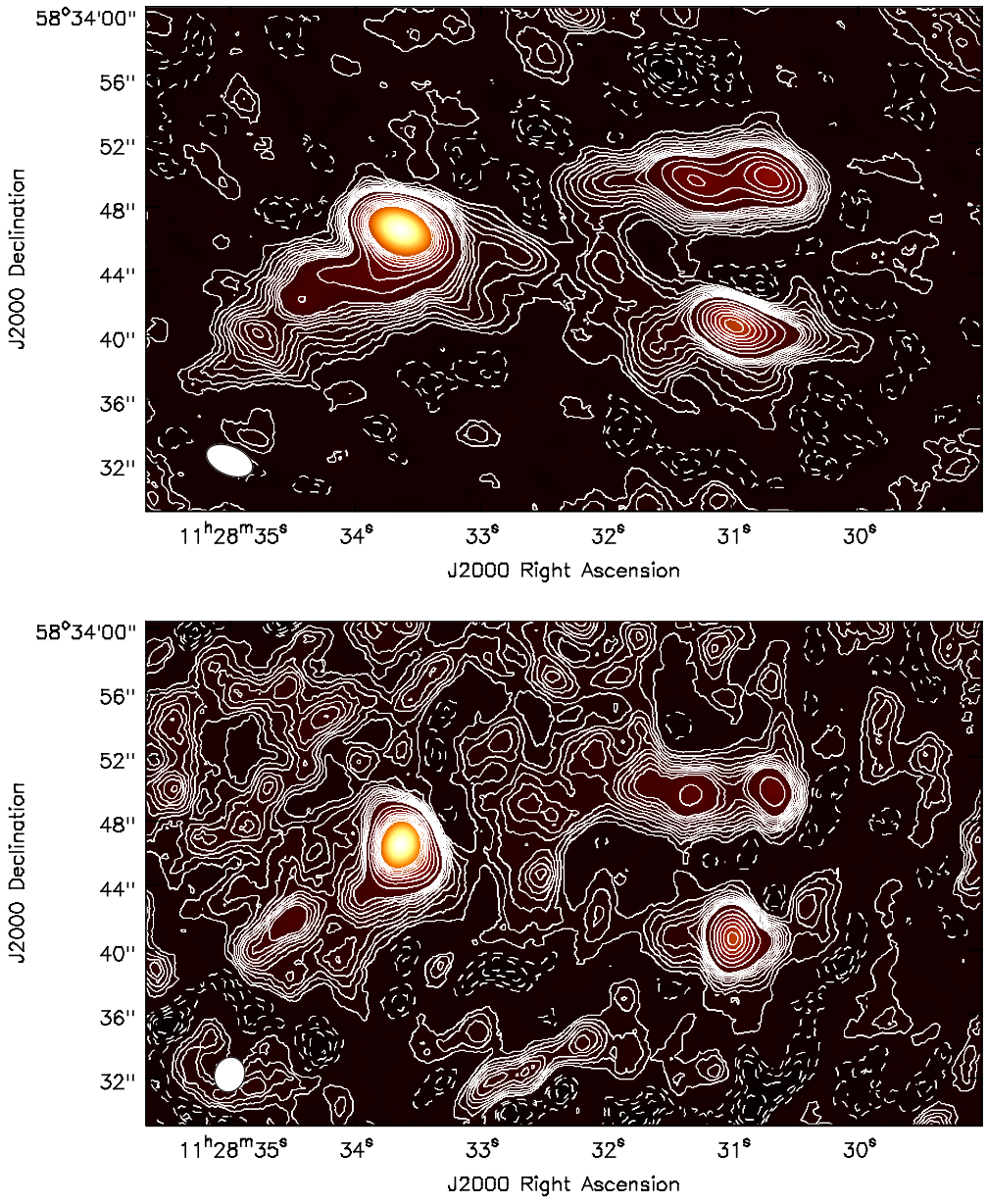

Figure 2.10 Feathered SMA maps: (*top*) ^{12}CO J=2-1 map with contour levels as in Figure 2.3; (*bottom*) ^{12}CO J=3-2 map with contour levels as in Figure 2.5

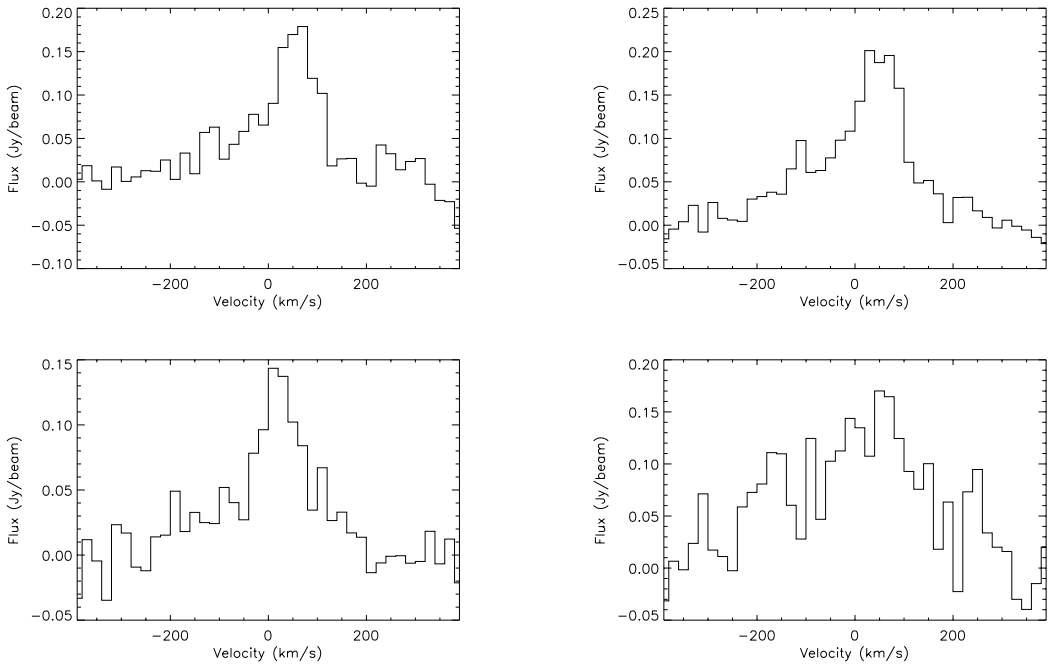

Figure 2.11 ^{12}CO J=3-2 spectra of enhanced emission regions after feathering: (*top left*) region at RA=11:28:33 Dec=+58d33m51, (*top right*) region at RA=11:28:32 Dec=+58d33m42, (*bottom left*) region at RA=11:28:32 Dec=+58d33m40 (*bottom right*) region at RA=11:28:34 Dec=+58d33m47 north east of IC 694 shows no obvious line and is likely to be an artifact.

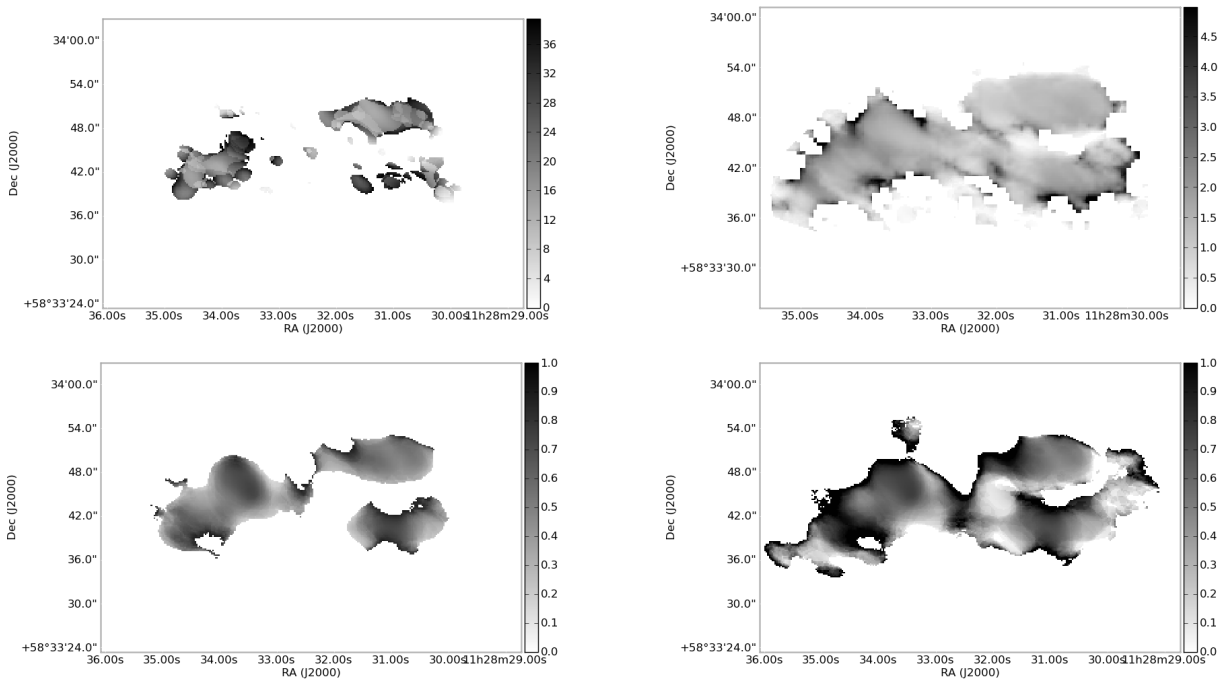

Figure 2.12 Line ratio maps: (*Top Left*) ^{12}CO/^{13}CO; (*Top Right*): 2-1/1-0 ; (*Bottom Left*): SMA only 3-2/2-1; (*Bottom right*): Feathered 3-2/2-1 ratio map

Chapter 3

Results

3.1 Line Ratios

Using the ratio maps (see Figure 2.12), we obtain the ratio values at the peak pixel of each region in the ^{12}CO J=3-2 map. The ratio and 1σ values are presented in Table 3.1. The 1σ values are calculated assuming a 20% calibration error for each map for the ^{12}CO $\frac{J=3-2}{J=2-1}$ and ^{12}CO $\frac{J=2-1}{J=1-0}$ and a 10% calibration error for each map for the $\frac{^{12}\mathrm{CO}}{^{13}\mathrm{CO}}$ J=2-1 ratio since these maps were observed simultaneously. The $\frac{^{12}\mathrm{CO}}{^{13}\mathrm{CO}}$ J=2-1 ratios reveal that regions A and B have similar physical conditions and regions C and A$'$ have similar physical conditions. We see that including short spacings with the JCMT maps does not change the peak ratio values significantly for each major region except for the disk portion of region A. It is interesting to see that before correcting for missing short spacings, the physical conditions of the disk portion of region A are similar to those of region C.

Our interferometric ^{12}CO $\frac{J=3-2}{J=2-1}$ ratio values are the first for Arp 299. Aalto et al. (1995) calculated CO line ratios for Arp 299 using the 12 m NRAO

observatory. With the poor resolution, line ratios for each individual region were difficult to obtain. They find the following line ratios : ^{12}CO $\frac{J=2-1}{J=1-0} = 0.95$ ± 0.06, $\frac{^{12}\mathrm{CO}}{^{13}\mathrm{CO}}$ J=1-0 ≥ 19, $\frac{^{12}\mathrm{CO}}{^{13}\mathrm{CO}}$ J=2-1 $=17 \pm 2$ and ^{13}CO $\frac{J=2-1}{J=1-0} \geq 1.2$ for region A. We see that the ^{12}CO $\frac{J=2-1}{J=1-0}$ line ratio differs from our own value greatly (see Table 3.1). This could be explained by a line ratio gradient. Our ^{12}CO $\frac{J=2-1}{J=1-0}$ line ratio does not include short spacings making the value sensitive only to small scale structures. Aalto et al. (1997) used the OVRO to calculate line ratios. They found $\frac{^{12}\mathrm{CO}}{^{13}\mathrm{CO}}$ J=1-0 that ranged from 10 ± 3 (region C) to 60 $\pm$ 15 (region A). Aalto et al. (1997) suggest that the unusually high (> 20) $\frac{^{12}\mathrm{CO}}{^{13}\mathrm{CO}}$ J=1-0 line ratios are due to a small or moderate optical depth ($\tau \leq 1$) in the ^{12}CO J=1-0 line. Our ^{12}CO $\frac{J=2-1}{J=1-0}$ line ratios also indicate that the ^{12}CO J=1-0 line has an optical depth of less than 1 (i.e. optically thin) which is quite unusual.

Casoli et al. (1999) used the PdB combined with the IRAM 30m dish to calculate similar line ratios to those of Aalto et al. (1997). They found $\frac{^{12}\mathrm{CO}}{^{13}\mathrm{CO}}$ J=1-0 line ratios of 24 ± 2 for region A, 29 ± 3 for region B, 16 ± 1 for region C and 10 ± 1.5 for region A$'$. These ratio values are very similar to what we find with $\frac{^{12}\mathrm{CO}}{^{13}\mathrm{CO}}$ J=2-1 and are quite different from what Aalto et al. (1997) found. Casoli et al. (1999) suggests that the difference in the line ratios arises from the way the continuum subtraction is performed. They suggest that Aalto et al. (1997) may have removed too much continuum for region A from their ^{13}CO J=1-0 map giving rise to a larger line ratio although they do warn that it is difficult to compare the two results because their maps include short spacings.

Table 3.1. CO Line Ratios

Region	^{12}CO $\frac{J=3-2}{J=2-1}$ [a]	^{12}CO $\frac{J=3-2}{J=2-1}$ [b]	^{12}CO $\frac{J=2-1}{J=1-0}$	$\frac{^{12}\mathrm{CO}}{^{13}\mathrm{CO}}$ J=2-1
A (IC 694)	0.74 ± 0.21	0.71 ± 0.20	1.45 ± 0.41	30.9 ± 4.4
B (NGC 3690)	0.72 ± 0.20	0.73 ± 0.21	1.77 ± 0.50	27.3 ± 3.9
C (Overlap)	0.51 ± 0.15	0.52 ± 0.15	1.50 ± 0.42	17.2 ± 2.4
A′ (IC 694 Disk)	0.77 ± 0.22	0.58 ± 0.16	1.54 ± 0.44	12.6 ± 1.8

[a]Using feathered maps

[b]Using SMA only maps

3.2 Properties

The dynamical mass, M_{dyn}, of each region can be calculated using the ^{12}CO J=3-2 map which has the best resolution and the equation from Wilson & Scoville (1990)

$$M_{dyn} = 99\Delta V^2_{FWHM} D(\mathrm{pc}) M_\odot \tag{3.1}$$

where ΔV_{FWHM} is the CO line full width half-maximum in km s^{-1} and D(pc) is the diameter of the cloud/region in pc. The velocity line width FWHM of each region was fitted to a Gaussian and the results are presented in Table 3.2. The FWHM values are quite consistent through each map. The size of each region was obtained by fitting to a two dimensional Gaussian. The source sizes listed in Table 3.3 are deconvolved from the beam size and measured in the ^{12}CO J=3-2 map (the best resolution map). Using the dynamical masses and source sizes, we can put an upper limit to the column density of ^{12}CO using the prior in Panuzzo et al. (2010)

Table 3.2. Fitted Gaussian Line Width (FWHM) for each region

	FWHM (km s^{-1})			
Region	^{12}CO J=1-0	^{12}CO J=2-1	^{13}CO J=2-1	^{12}CO J=3-2
A	290	310	290	325
B	185	180	150	185
C	80	80	70	80
A′	90	90	100	90

Table 3.3. Deconvolved Gaussian Source Sizes

Region	FWHM (arcsec)	FWHM (parsec)
A	1.7 × 1.2	360 × 260
B	2.0 × 1.4	430 × 300
C	10 × 1.6	2100 × 340
A′	6.1 × 2.3	1300 × 490

$$\mathrm{N}(^{12}\mathrm{CO}) < \frac{M_{dyn} x_{CO}}{m_{H_2} \mu} \times \frac{1}{\pi R^2} \tag{3.2}$$

where x_{CO} is the abundance of CO relative to H_2, $x_{CO} = 3 \times 10^{-4}$ (Ward et al. 2003), m_{H_2} is the mass of a molecular hydrogen molecule, μ is the mean molecular weight in units of m_{H_2} (=1.4) and R is the radius of the region. This prior assures us that the ^{12}CO column density obtained from the radiative transfer fits does not exceed the dynamical mass of each region (see Table 3.4).

Table 3.4. Dynamical Masses and Priors

Region	M_{dyn} ($M_\odot$)	Diameter (pc)	Column Density Prior (cm^{-2})
A	3.2×10^9	300	6.2×10^{20}
B	1.3×10^9	360	1.7×10^{20}
C	5.0×10^8	845	1.2×10^{19}

3.3 RADEX

To constrain the temperature and density of each region, we use the radiative transfer code RADEX (van der Tak et al., 2007). RADEX is a simple radiative transfer code that assumes a homogeneous medium making it a useful tool to constrain the physical conditions such as density and temperature using observational data. The user must input a molecular column density ($N(\mathrm{cm}^{-2})$), the collision partner (i.e. H_2) and its density ($n(H_2)$), kinetic temperature (T_{kin}) and line width (km s^{-1}) for the particular observation (see appendix B for more details). The code was run for each region and the disk portion of region A. We created a 3D grid of models varying $N(^{12}\mathrm{CO})$ in steps of 0.1×10^{18} cm^{-2}, T_{kin} in steps of 1K and $\log(n(\mathrm{H_2}))$ in steps of 0.02. The input for each region is presented in Table 3.5. We use a ^{12}CO to ^{13}CO abundance ratio of 50. The RADEX solutions were plotted with T_{kin} vs. $n(H_2)$ for the appropriate line ratio and $\pm 1\sigma$. The solutions are picked out where the three line ratios overlap within the $\pm 1\sigma$ by inspection by eye (see Figure 3.1). For region A, A$'$ and B we see two situations, a density constrained with temperature unconstrained solution and a temperature constrained with

Table 3.5. Radex INPUT Parameters

				Linewidth (dV)	
Region	T_{kin} (K)	$\log(n(H_2))$ (cm^{-3})	$N(^{12}CO)$[a] ($\times 10^{18}$ cm^{-2})	^{12}CO (km s^{-1})	^{13}CO (km s^{-1})
A	10-1000	2-8	0.9 - 50	325	325
B	10-1000	2-8	0.9 - 50	185	185
C	10-500	2-8	0.8 - 5	80	80
A′	10-1000	2-8	0.9 - 50	90	90

[a]Abundance ratio of $[^{12}CO]/[^{13}CO] = 50$ was used to determine $N(^{13}CO)$

density unconstrained solution. For region C, we have a constrained solution for both temperature and density. The solutions are summarized in Table 3.6. We discuss the solutions in Chapter 4.

Table 3.6. Radex Results

Region	$N(^{12}CO)$ (cm^{-2})	T_{kin} (K)	$n(H_2)$ (cm^{-3})	τ_{1-0}	τ_{2-1}	τ_{3-2}
A	1-10 $\times$ 10^{18}	15-500	$>10^{2.5}$	-	-	-
B	1-6 $\times$ 10^{18}	15-1000	$>10^{2.5}$	-	-	-
C	0.9-2 $\times$ 10^{18}	10-30	$10^{3.5-4.5}$	$\sim$0.8 -0.95	$\sim$2-2.5	$\sim$2.3
A′	2-30 $\times$ 10^{18}	20-500	$>10^{2.5}$	-	-	-

3.4 Star Formation Rates and Depletion Times

The star formation rate is a useful quantity that allows us to measure the amount of gas mass used up each year in order to create new stars. The problem with most star formation tracers is that they require an estimate of the amount of extinction. U/LIRGs are quite dusty and may have $A_v \sim 1000$ mag (Hinz & Rieke, 2006). Since extinction is less important towards longer wavelengths, we use the infrared luminosity of each region to determine the star formation rate. Charmandaris et al. (2002b) estimated the infrared luminosity of each region in Arp 299 using published mid-infrared and far-infrared fluxes to create a spectral energy distribution (SED) for each region. The SEDs were modeled with two modified blackbody functions with a spectral index of 1.5. To estimate the infrared luminosities, the SEDs were integrated (see Table 3.7).

Alonso-Herrero et al. (2000) also have made estimates of the infrared luminosities of each region. Instead of a SED fit, Alonso-Herrero et al. (2000) estimated the fraction of the total infrared luminosity from each region derived from ground-based mid-infrared observations. From the relative fluxes at 10, 12, 20 and 30 μm through a 6″ diameter, they estimate that region A is about 50% of the total infrared luminosity, region B is about 27% and region C is about 13%. The final 10% is believed to be associated with H II regions. If Arp 299 has a far-infrared infrared luminosity of $5.5 \times 10^{11}\ L_{\odot}$, we use these fractions to estimate the far-infrared luminosity of each region (see Table 3.7). Alonso-Herrero et al. (2000) also made estimates of the dynamical mass and

Table 3.7. Published Properties

Region	M_{dyn}[a] ($M_\odot$)	L_{IR}[c] ($L_\odot$)	L_{FIR}[b] ($L_\odot$)	A_v[a] (mag)
A	5.8×10^9	1.8×10^{11}	2.75×10^{11}	17
B	$\sim 1 \times 10^9$	9.4×10^{10}	1.49×10^{11}	11
C	$> 0.3 \times 10^9$	4.4×10^{10}	0.72×10^{11}	15

[a]Published in Alonso-Herrero et al. (2000)

[b]Calculated using the infrared luminosity fraction of Alonso-Herrero et al. (2000) and $L_{FIR} = 5.5 \times 10^{11}\ L_\odot$ for Arp 299

[c]Published in Charmandaris et al. (2002b)

visual extinction of each region. The dynamical mass was estimated using the CO absorption lines in the near-infrared. The dynamical mass values we obtain from our CO observations agree well with Alonso-Herrero et al. (2000). The visual extinction was estimated using a screen model with H recombination lines (Alonso-Herrero et al., 2000).

The molecular gas mass of each region can be calculated using the ^{12}CO J=1-0 map and the equation

$$\frac{L'_{CO}}{\text{K km s}^{-1}\text{ pc}^2} = 3.2546 \times 10^7 \left(\frac{S_{CO}}{\text{Jy km s}^{-1}}\right) \left(\frac{D_L}{\text{Mpc}}\right)^2 \left(\frac{\nu_o}{\text{GHz}}\right)^{-2} (1+z)^{-1} \tag{3.3}$$

where S_{CO} is the flux of the CO line in Jy km s^{-1}, D_L is the luminosity distance in Mpc, ν_o is the rest frequency of the CO line in GHz and z is the redshift (Wilson et al., 2008). Since the ^{12}CO J=1-0 map does not include short spacing and we do not know how much flux is missing, we use the feathered ^{12}CO J=2-

1 map to measure the gas masses of each region. We use an average ratio value of $^{12}\mathrm{CO}\frac{J=2-1}{J=1-0}$ =1.4 to estimate the gas mass given by

$$M(H_2) = 0.57 L'_{COJ=2-1} \tag{3.4}$$

where $L'_{COJ=2-1}$ is given by Equation 3.3. Using the total molecular mass and star formation rates of each region, we can estimate the amount of time it will take for all the gas to be depleted by star formation using

$$t_{depl} = \frac{1.36 M(H_2)}{\dot{M}_{SFR}} \tag{3.5}$$

where the factor 1.36 is to account for the He gas. The star formation rate can be estimated using the equation from Kennicutt (1998) and the infrared luminosity (8-1000μm)

$$\dot{M}_{SFR}(M_\odot \text{ yr}^{-1}) = 4.5 \times 10^{-44} L_{IR}(\text{erg s}^{-1}). \tag{3.6}$$

Kennicutt (1998) used a Salpeter initial mass function (IMF) to estimate the star formation rate which is seldom used anymore. Calzetti et al. (2007) used a double power law IMF with a slope of -1.3 in the range of 0.1-0.5 $M_\odot$ and a slope of -2.3 in the range of 0.5-120 $M_\odot$ to derive a star formation rate. They found that the star formation rate is 1.59 times lower than the star formation rate determined using the Salpeter IMF.

In order to minimize any contribution to the infrared luminosity from any AGNs present in Arp 299, we adopt the method by Genzel et al. (2010). Genzel et al. (2010) have taken the far-infrared luminosity of their sources and multiplied by 1.3 to estimate the total infrared (8-1000μm) luminosity associated with star formation. This method avoids using the mid-infrared

luminosity that is more likely to be contaminate by an AGN. The correction factor of 1.3 is an average L_{IR}/L_{FIR} in nearby star-forming galaxies (Graciá-Carpio et al., 2008). We can simply update Equation 3.6 to

$$\dot{M}_{SFR}(M_\odot \text{ yr}^{-1}) = 1.4 \times 10^{-10} L_{FIR}(L_\odot). \tag{3.7}$$

We use $L_{FIR} = 5.5 \times 10^{11}$ $L_\odot$ (Sanders et al., 2003) for Arp 299 and the fractions of the total luminosity of Alonso-Herrero et al. (2000) to estimate the far-infrared luminosity of each region. Table 3.8 summarizes the derived properties of Arp 299. We discuss the star formation rates and depletion times in Section 4.2. When we compare our gas masses to the dynamical masses, we see that regions A and B have about 20% gas mass and region C has about 68%. If we were to derive gas masses using the standard Galactic conversion factor, 3.2 $M_\odot$ (K km s^{-1} pc^2)$^{-1}$, our gas masses would be about 4 times higher. That would push the $M(H_2)/M_{dyn}$ ratios to about 80% for regions A and B and to 280% for region C. The gas masses derived using the standard Galactic conversion factor are not likely especially for region C because the gas mass cannot be greater than the dynamical mass. As for regions A and B, 80% gas mass is very unlikely because we know that these regions contain AGNs and super star clusters.

Alonso-Herrero et al. (2000) observed Arp 299 in Paα which can be used as a star formation tracer. The only problem with this tracer is the estimation of the amount of extinction. We use the extinction values given in Alonso-Herrero et al. (2000) (see Table 3.4) and the Paα emission from a 5″ aperture to estimate the star formation rates. To correct for extinction we use

$$F_{\lambda,0} = F_\lambda 10^{0.4A(\lambda)} \tag{3.8}$$

Table 3.8. Gas Mass and Depletion Times

Region	$\dot{M}_{SFR}$ ($M_\odot$ yr^{-1})	Flux (Jy km s^{-1})	L_{CO}[a] (K km s^{-1} pc^2)	M(H_2) ($M_\odot$)	t_{depl} (Myr)
A	38.5	918 ± 110	1.1×10^9	6.2×10^8	22
B	20.9	392 ± 35	4.6×10^8	2.6×10^8	17
C	10.1	505 ± 28	5.9×10^8	3.4×10^8	46
A′	<7.7[b]	319 ± 16	3.8×10^8	2.2×10^8	>25
Total	77	2382 ± 23	2.8×10^9	1.6×10^9	29

[a]Using D_L=44 Mpc

[b]$\dot{M}_{SFR}$ calculated assuming the region is 10% the total infrared luminosity of Arp 299.

where $F_{\lambda,0}$ is the extinction corrected flux, F_λ is the flux that is observed and $A(\lambda)$ is the magnitude extinction value for that specific wavelength, λ which is given to be $0.128A_v$ (Alonso-Herrero et al., 2000) for Paα.

Alonso-Herrero et al. (2006) use the star formation rate using Hα published in Kennicutt (1998) to estimate a star formation rate using the ratio Paα/Hα = 8.6 from Hummer & Storey (1987) to get

$$\dot{M}_{SFR} = 6.79 \times 10^{-41} L_{Pa\alpha} (\text{erg s}^{-1}) \tag{3.9}$$

Again, we need to correct this estimate by a factor of 1.59 to convert to the double power law IMF. Table 3.9 presents the star formation rated derived from Pa α emission. We see that the star formation rates for region A and B are somewhat lower than what we estimate using the infrared luminosity. This may be due to underestimated extinction values and can be used as lower limits to the star formation rates. The star formation rate for region C is much

Table 3.9. Paα Properties

Region	Flux [a] (erg cm^{-2} s^{-1})	$L_{Pa\alpha}$ (erg s^{-1})	$\dot{M}_{SFR}$ ($M_\odot$ yr^{-1})	t_{depl} (Myr)
A	3.7×10^{-13}	6.4×10^{41}	27.4	23
B	2.3×10^{-13}	1.9×10^{41}	8.3	31
C	4.4×10^{-13}	5.9×10^{41}	25.3	13

[a]Flux from a 5″ aperture given in Alonso-Herrero et al. (2000)

higher than what we derive using the infrared luminosity. The aperture size may be too large and likely includes flux from region B.

3.5 Average Density for Region C

Since region C has a well constrained radiative transfer solution, we can compare the solution's column density to the average column density within the beam. Using the feathered ^{12}CO J=2-1 map, the peak value in region C is 133 Jy/beam km s^{-1} with a beam size of 3.0″ × 1.8″. Using Equation 3.3, we get $L'_{CO} = 1.6 \times 10^8$ K km s^{-1} pc^2 which corresponds to a mass of $M_{H_2} = 8.95 \times 10^7$ $M_\odot$ using equation 3.4. Using the equation

$$N(H_2) = \frac{M_{H_2}}{m_{H_2}} \frac{1}{\text{beam area}} \tag{3.10}$$

where beam area = $1.133\theta_{major} \times \theta_{minor}$, we calculate an average H_2 column density of 2×10^{22} cm^{-2}. Using the ^{12}CO column density obtained from the RADEX solution, we get a ^{12}CO abundance of N(^{12}CO)/N(H_2) = 0.5 - 1.0 ×

10^{-4}. This is about 3 - 6 times lower than the abundance ratio of 3×10^{-4} that is typically assumed. We discuss the implications in Section 4.1.

We can also calculate the average volume density of region C assuming a spherical geometry. The radius of region C is R $\sim$ 420 pc and the molecular gas mass is given in Table 3.8. Using the equation

$$< n(H_2) >= \frac{M_{H_2}}{m_{H_2}} \frac{3}{4\pi R^3} \tag{3.11}$$

we derive an average volume density of 22 molecules cm^{-3}. Comparing this average value to the RADEX solution $n(\mathrm{H_2})$ suggests that the cloud is diffuse with some fraction being dense, a similar structure to giant molecular clouds in the Galaxy.

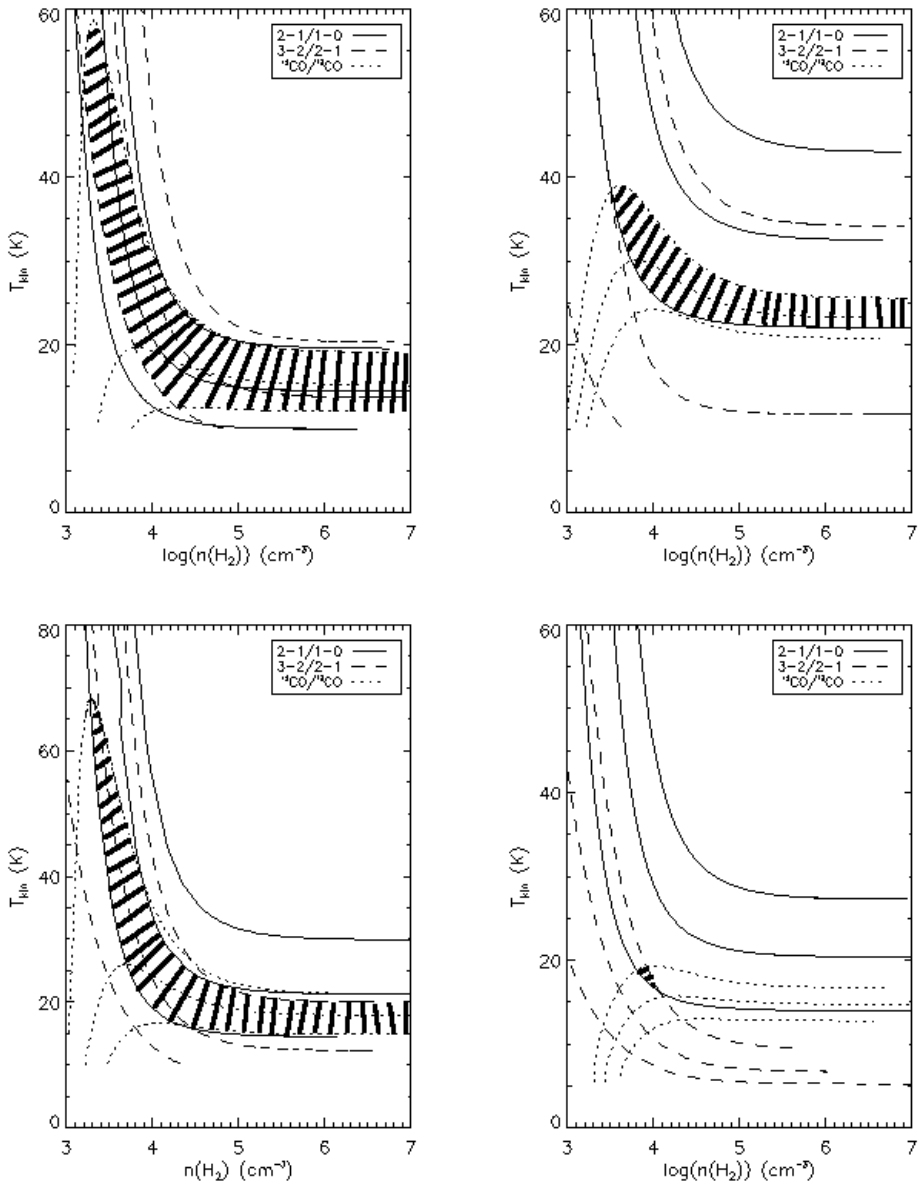

Figure 3.1 Sample RADEX plots of each region of Arp 299: (*top left*) Region A for $N(^{12}\mathrm{CO}) = 2.1 \times 10^{18}$ cm $^{-2}$, (*top right*) Region A′ for $N(^{12}\mathrm{CO}) = 4 \times 10^{18}$ cm $^{-2}$, (*bottom left*) Region B for $N(^{12}\mathrm{CO}) = 2.0 \times 10^{18}$ cm $^{-2}$ and (*bottom right*) Region C for $N(^{12}\mathrm{CO}) = 1.3 \times 10^{18}$ cm $^{-2}$. The thick solid lines denote solutions.

Chapter 4

Discussion

4.1 x_{CO} Value for Region C

In section 3.5, we calculated the average H_2 column density for region C and compared it to the RADEX ^{12}CO column density solution to derive a CO-to-H_2 abundance, x_{CO}. Our derived factor is about 3 - 6 times less than the assumed value of 3×10^{-4}, the average Galactic value. This difference may be interpreted in two ways. One explanation can be that the abundance of ^{12}CO to H_2 is different in this region of Arp 299 than the average Galactic value. Another explanation is, if we assume that the Galactic value is correct for this region of Arp 299, then the column density estimated with α ($=M_{H_2}/L'_{CO}$) is too high, which means that the value of α is smaller than 0.8 $M_\odot$(K km s^{-1} pc^2)$^{-1}$. There is no way of telling which scenario is right and it may be a combination of the two.

4.2 Depletion Times

The depletion times of each region (see Table 3.8) are quite fast compared to normal spiral galaxies. The timescales are more similar to the lifetime of a giant molecular cloud in the Large Magellenic Cloud (20-30 Myr; Kawamura et al., 2009). This leads to the question whether the star formation rates are over estimated due to contributions from AGNs. Daddi et al. (2010) studied the star formation laws in disks and starbursts at low and high redshifts. They provide evidence that disks and starbursts occupy distinct regions in the gas mass versus star formation rate (or L_{IR}) plane (see Figure 4.1). Starbursts are seen to have 10 times higher L_{IR} at fixed M_{gas}. From the plot, we can see that U/LIRGs have depletion times on the order of 10^7 years while spiral galaxies have depletion times in the range of 0.6 - 2.4 Gyr. Around the same time, Genzel et al. (2010) also find the same bimodal trend. This trend could be explained by an IMF that is more top heavy than in normal disk galaxies (Daddi et al., 2010; Genzel et al., 2010). Genzel et al. (2010) argues that there is no convincing evidence in the local Universe for this situation except in the vicinity of the black hole in the Galactic center; therefore this explanation is unlikely but cannot be ignored until further observational evidence is presented.

This bimodal trend is shown to disappear when the gas masses are divided by the dynamical times, τ_{dyn} by both Daddi et al. (2010) and Genzel et al. (2010) (see Figure 4.2). This is the first time that global galaxy properties that determine τ_{dyn} are shown to be related to the regulation to the local process like star formation. This interesting result suggests that a difference in IMFs

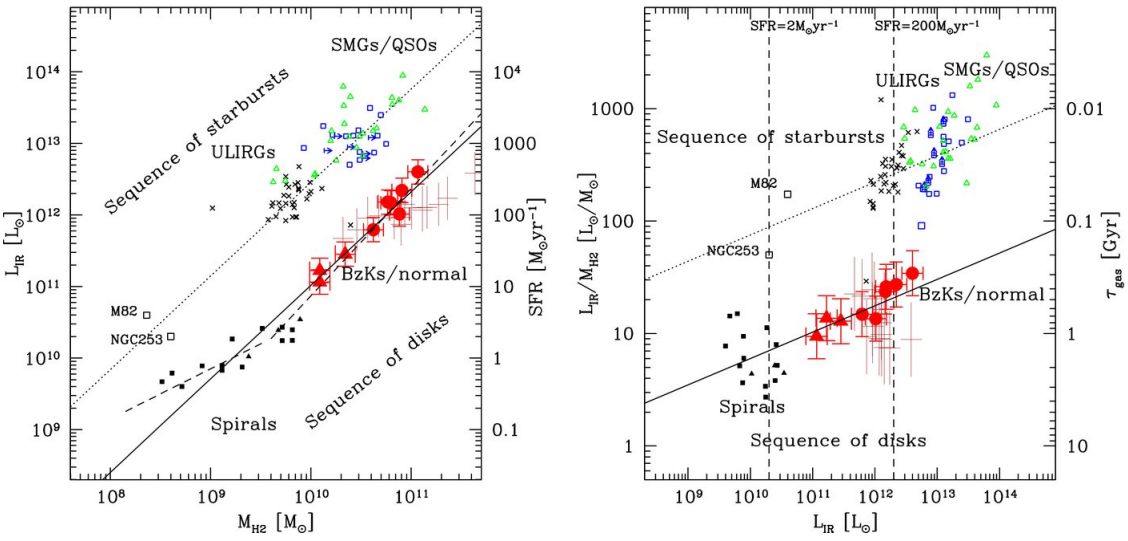

Figure 4.1 Comparison of the molecular gas masses and infrared luminosity (or $\dot{M}_{SFR}$) of local spirals (black filled squares and triangles), z $\sim$ 0.5 disk galaxies (red filled triangles), z =1-2.3 normal galaxies (brown crosses), SMGs (blue squares), QSOs (green triangles), and local ULIRGs (black crosses) taken from Daddi et al. (2010)

cannot explain the trend as different IMFs would break the single relations found by using τ_{dyn} (Daddi et al., 2010). The most likely explanation is that mergers form stars much faster because the clouds are more compressed with shorter dynamical times so that they can use up the gas reservoir much more quickly than normal spiral galaxies. This explanation is consistent with the L_{IR} vs L_{HCN} linear correlation (Gao & Solomon 2004; see Chapter 1.1.2). Using this correlation, the bimodal trend can be seen as starbursts having a higher fraction of dense gas than normal disk galaxies at a fixed L_{IR}. This explanation may likely be the case for Arp 299 since our RADEX solutions show a cold dense gas for all regions.

In order to increase the depletion time to similar values of normal spiral galaxies, we need one of two things to happen: the molecular mass must be

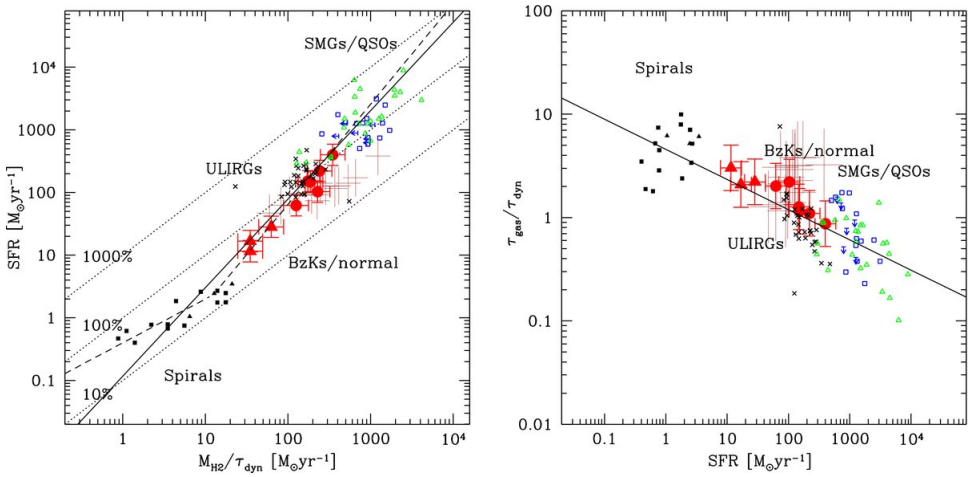

Figure 4.2 Same as Figure 4.1 but dividing the gas mass by an average estimate of the dynamical time for each population group taken from Daddi et al. (2010)

increased or the star formation rate must decrease. If the star formation rates are correct, to get depletion times on the order of a Gyr, we need molecular gas masses that are $> 10^{10}$ $M_{\odot}$. This is not possible because it exceeds the dynamical masses derived in Chapter 3.2. If the entire dynamical masses were purely due to molecular gas, the depletion times would increase by about 4 times for region A and B and by only about 1.1 for region C. These depletion time scales using the dynamical masses are still much lower than of a normal spiral galaxy. In the previous section, we showed that the abundance ratio α, may be smaller than the value of 0.8 $M_{\odot}$(K km s^{-1} pc^2)$^{-1}$ we use to derive molecular gas masses. This would mean that the gas masses we derive are overestimates and would also imply that our depletion timescales are overestimates.

If the gas masses are correct, then the star formation rates may be overestimated. If we assume that the AGNs contribute 50% to the total infrared luminosity, the depletion times scales are increased by 2. These timescales are

still much lower than of a normal spiral galaxy. To get the timescales up to 1 Gyr, the AGN contribution must be greater than 95%. This is highly unlikely considering the evidence for a star formation powered system (see Chapter 1). As for region C, no AGN is associated with this region; therefore the total infrared luminosity must be due to star formation. This is quite an interesting region considering that region C is not associated with the nucleus of another galaxy but has a star formation rate much higher than a normal spiral galaxy.

4.3 RADEX Solutions

Our RADEX solutions for regions A, B and A′ show two situations, a density constrained with temperature unconstrained solution and a temperature constrained with density unconstrained solution. This can be interpreted as a double component solution with a moderately dense warm ($T_{kin} > 30$K) gas component and a dense cold ($T_{kin} \sim$ 10-30 K) gas component. Our observations likely do not trace the warm gas that is seen in the RADEX solutions because ^{12}CO J=3-2 traces gas temperatures of T $\sim$ 30 K; therefore we cannot say that there is a warm gas component from our solution but a warm gas cannot be ruled out. Higdon et al. (2006) has shown using mid-infrared *Spitzer* spectra that ULIRGs typically have less than 1% of warm ($T > 100$K) H_2 gas compared to the total H_2 gas mass traced by the ^{12}CO transition lines. This would indicate that Arp 299 could have about 2×10^7 $M_\odot$ of warm H_2 gas. If Arp 299 does have a warm component up to $T_{kin} \sim 500$ K, we would expect to see strong emission in higher J-level ^{12}CO lines in the *Herschel* FTS spectrum. The *Herschel* FTS spectrum for Arp 299 has not yet been published

; however, the data has become public. Taking a sneak peek at the spectrum shows a prominent ^{12}CO transition ladder with strong emission of higher J-level transition lines up to ^{12}CO J=13-12. A radiative transfer modelling solution of these CO transition lines would almost certainly show a warm/hot ($T_{kin} > 100$K) gas component as higher J-level transition lines probe regions of denser ($n(\mathrm{H_2}) \approx 3 \times 10^3 J^3$ cm^{-3}; see Tielens, 2005) and hotter gas ($T \approx 3J^2$ K).

RADEX modelling was performed with *Herschel* FTS observations for the prototype starburst M82 (Panuzzo et al., 2010). The spectrum shows a noticeable CO ladder from J=4-3 to 13-12 which indicates a warm gas component. Panuzzo et al. (2010) used a likelihood model and the spectrum of M82 with a 43″.4 beam to constrain the physical conditions. The most probable solution is $T_{kin} = 545$ K, $n(\mathrm{H_2}) = 10^{3.7}$ cm^{-3} and $N(^{12}\mathrm{CO}) = 10^{19}$ cm^{-2}. This solution is quite similar to the warm/hot gas solution that we see in the nuclei and the disk portion of IC 694. A cold component solution of $T_{kin} \sim 30$ K with $n(\mathrm{H_2}) = 2.5 \times 10^4$ cm^{-3} has also been found using ground based observations (Petitpas & Wilson, 2000) which is similar to what we see in our RADEX solutions for region C.

Local velocity gradient (LVG) modelling was also performed on a sample of seven GMCs in the normal spiral galaxy M33 (Wilson et al., 1997). The average of six clouds resulted in a solution of T_{kin} =10-20 K, $n(\mathrm{H_2})$ = 4-30 $\times$ 10^3 cm^{-3} and $N(^{12}\mathrm{CO})$ = 3-6 $\times$ 10^{17} cm^{-2}. This average solution resembles our RADEX solution for region C very well except the column density is lower. The column density solution from Wilson et al. (1997) is an average column

density over the size of the beam. We can determine the average column density over the cloud by determining the filling factor of the cloud within the beam

$$ff = \frac{D_{cloud}^2}{D_{beam}^2} \tag{4.1}$$

where D_{cloud} is the diameter of the cloud and D_{beam} is the physical diameter of the beam (=85 pc). Using the equation in Wilson & Scoville (1990)

$$V_{FWHM} = 1.2 D_{pc}^{0.5} \tag{4.2}$$

where V_{FWHM} is the line width FWHM of the CO line and D_{pc} is the diameter of the cloud in pc and using the average V_{FWHM} for the six clouds given in Wilson et al. (1997) (= 9.3 km s^{-1}), we get an average D_{cloud} = 60 pc. This gives us a filling factor of $ff = 0.5$ and a corrected column density of 6-12 $\times$ 10^{17} cm^{-2}. Converting this ^{12}CO column density to H_2 column density using $x_{CO} = 3 \times 10^{-4}$ we get $N(H_2)$ = 2-4 $\times$ 10^{21} cm^{-2}. Comparing this value to the RADEX solution's column density of region C, we see that region C has about 1.7-3.3 times the average column density of the six clouds in M33 in a 500pc region. This would imply that the beam is filled with clouds spaced close together and likely that there exists a large number of dense gas regions which could help explain the short depletion time and high star formation rate.

We can also compare the average volume density we estimated in Chapter 3.5 to the average value of the six clouds in M33. Using the equation given in Wilson & Scoville (1990)

$$< n(H_2) >= 200 (D_{pc}/20pc)^{-1} \tag{4.3}$$

and the average cloud diameter, we get an average volume density of about 67 molecules cm^{-3} for the clouds in M33. This is about 3 times larger than the value of region C. Using Equation 4.3, we see that the average volume density for region C corresponds to what we would except for a giant molecular cloud with a diameter of 200 pc. Region C is much larger than 200 pc which would imply that region C is in some sense overdense. However, for region C, we do not know the third dimension to get a proper volume. Our volume estimate is most likely to be overestimated and the average volume density is underestimated. If we use R=300 pc, we get an average volume density of 62 cm^{-3} which is similar to the clouds of M33. This would imply that region C is similar to a 60 pc giant molecular cloud but on a larger scale. From the column density comparison, we see that looking at a line of sight, we will encounter a maximum 3 giant molecular clouds of about D=60 pc. We can use this to estimate the thickness of region C. If each cloud has a diameter of 60 pc and the space in between clouds are negligible, we can estimate the thickness to be 180 pc. Using the size of region C and this thickness we get an average volume density of about 100 cm^{-3}. This would imply that region C is much denser than a 60 pc cloud in M33 on a much larger scale!

Recently, RADEX modelling of the "prototypical" ULIRG Arp 220 using FTS *Herschel* data and a likelihood code was shown to have a two component molecular gas (Rangwala et al., 2011), just as was shown in M82. The most probable solution for the warm component was $T_{kin} \sim 1340$ K, $n(H_2) = 10^{3.2}$ cm^{-3} and $N(^{12}CO) = 10^{19.4}$ cm^{-2} and for the cold component $T_{kin} \sim 50$ K, $n(H_2) = 10^{2.8}$ cm^{-3} and $N(^{12}CO) = 10^{20.3}$ cm^{-2}. These gas components are hotter and $N(^{12}CO)$ is higher than what we find for Arp 299. This difference

may be because Arp 220 is in a later stage of the merger than Arp 299 where the nuclei are separated by 300 pc (Scoville et al., 1997).

Rangwala et al. (2011) have shown that the mid-J to high-J CO transition lines are tracing the warm/hot gas and the low-J CO transition lines are tracing the cold gas ($T \sim 50$ K). This indicates that the ^{12}CO J=3-2 transition line may not be tracing the hot gas component as we assumed earlier. In order to trace the warm/hot gas component we need to observe Arp 299 in higher ^{12}CO transition lines.

Chapter 5

Conclusions

We have analyzed the interferometric CO observations of the local LIRG Arp 299 published in Wilson et al. (2008). CO transition line ratios were used to constrain the physical conditions of each region of Arp 299 using the radiative transfer code RADEX. The RADEX solutions show two situations for regions A, A′ and B, where one of either temperature or density is constrained and the other is not. The RADEX modelling shows a solution for $T_{kin} \sim$ 30-500 K (up to 1000 K for region B) and $n(\mathrm{H_2}) \sim 0.3$ - 3 $\times$ 10^3 cm^{-3} and $T_{kin} \sim$ 10-30 K and $n(\mathrm{H_2}) > 3 \times 10^3$ cm^{-3}. This indicates a two component gas but our ^{12}CO J=3-2 observations likely do not trace the warm gas component and we need higher J-level ^{12}CO transition lines to trace the warm gas. We cannot rule out a warm/hot gas solution. Region C corresponding to the overlap region of Arp 299 shows a well-constrained RADEX solution with $T_{kin} \sim$ 15-30 K, $n(\mathrm{H_2}) \sim 3$ - 30 $\times$ 10^3 cm^{-3} and $N(^{12}\mathrm{CO}) \sim 0.9$-2 $\times$ 10^{18} cm^{-2}. This solution is comparable to giant molecular clouds in the normal spiral galaxy M33. The column densities of these clouds (corrected with a filling factor), is about 1.7-3.3 times lower than the RADEX solution column density for region C which may indicate that clouds are spaced close together in region C.

We have used the CO observations to calculate the gas and dynamical masses of each region. We find that region A has $M(\mathrm{H_2}) = 6.2 \times 10^8\ M_\odot$ and $M_{dyn} = 3.2 \times 10^9\ M_\odot$, region B has $M(\mathrm{H_2}) = 2.6 \times 10^8\ M_\odot$ and $M_{dyn} = 1.3 \times 10^9\ M_\odot$, and region C has $M(\mathrm{H_2}) = 3.4 \times 10^8\ M_\odot$ and $M_{dyn} = 0.5 \times 10^9\ M_\odot$. Using the infrared luminosity we derived the star formation rate of each region to be 38.5 $M_\odot$ yr^{-1} for region A, 20.9 $M_\odot$ yr^{-1} for region B and 10.1 $M_\odot$ yr^{-1} for region C. We found that the depletion times of each region are about 2 orders of magnitude lower than for normal spiral galaxies and resemble the depletion timescales of giant molecular clouds. The lower timescales may be explained by a higher fraction of dense gas than in normal spiral galaxies.

As for future work, this project can be improved by obtaining another ^{13}CO transition line observation in order to better constrain the physical conditions. Another possibility to constrain the physical conditions is to obtain a dense gas tracer such as HCO+ or HCN; however adding these lines into our RADEX models will introduce more uncertainties because we are assuming another H_2 abundance ratio. The analysis can further be improved by recovering the short spacings of the ^{12}CO J=1-0 and ^{13}CO J=2-1 maps. We have proposed to observe Arp 299 in ^{13}CO J=2-1 using the JCMT but the observations are currently not complete. In order to determine if the merger state has an effect on the physical conditions, more RADEX modelling of U/LIRGs needs to be done. The sample of Wilson et al. (2008) has 13 other U/LIRGs that have not been analyzed in great detail.

Appendix A

Miriad to CASA Comparison

CASA (Common Astronomy Software Applications) is a data analysis software package that is currently being developed for the next generation of radio telescopes, specifically ALMA and the EVLA [1]. The package can process both single dish and interferometric data. It is worthwhile to compare this new package to an older, more familiar package such as Miriad. We shall use the feathering technique of combining the JCMT single dish data with the interferometric SMA data of each package to compare the two.

A.1 Miriad

The JCMT single dish data was binned to 20 km/s (optical definition) starting at -389.9 km/s using the JCMT software, *Starlink*. The data cube was converted to a fits file, imported into Miriad and was prepared for combination with the SMA map. The intrinsic unit of the JCMT data is antenna temperature (T_A) and was converted to main beam temperature (T_{mb}) using equation 2.2 since the emission fills the beam of the JCMT. The SMA data

[1] http://casaguides.nrao.edu/index.php?title=What_is_CASA%3F

has units of Jy/beam, so we converted the JCMT data to the unit of Jy/beam using equation 2.3 using η_{mb} =0.6 for ν =345GHz. The header was modified to include the beam information and rest frequency. The SMA data uses the radio definition of velocity, so the JCMT data was converted to this definition using the `velsw` task. The channels need to increase in velocity so the `reorder` task is used to rearrange the data cube. The following is the script used to prepare the JCMT map.

```
fits in=Arp299co32.sub20.JCMT.K.fits op=xyin out=Arp299co32.JCMTsub20.TAmiriad

##Convert Ta* to Tmb by dividing by eta_mb =0.6 for JCMT at CO(3-2)
maths exp='Arp299co32.JCMTsub20.TAmiriad/0.6'
out=Arp299co32.JCMTsub20.Tmbmiriad

####Convert from K to Jy/BEAM using 2.786x10^7/(Area(cm^2)*eta_mb) = 26.28
####Area = pi*(750cm)^2
maths exp='Arp299co32.JCMTsub20.Tmbmiriad*26.28'
out=Arp299co32.JCMTsub20.JyBEAMmiriad

###Fix the header information
puthd in=Arp299co32.JCMTsub20.JyBEAMmiriad/bunit value=JY/BEAM
puthd in=Arp299co32.JCMTsub20.JyBEAMmiriad/bmaj value=0.000067874
puthd in=Arp299co32.JCMTsub20.JyBEAMmiriad/bmin value=0.000067874
puthd in=Arp299co32.JCMTsub20.JyBEAMmiriad/bpa value=0
puthd in=Arp299co32.JCMTsub20.JyBEAMmiriad/btype value=Intensity type=ascii
```

```
puthd in=Arp299co32.JCMTsub20.JyBEAMmiriad/restfreq value=342.3 type=real
puthd in=Arp299co32.JCMTsub20.JyBEAMmiriad/ctype3 value=FELO-LSR

###Need to transform the optical velocity to the radio definition of velocity
velsw in=Arp299co32.JCMTsub20.JyBEAMmiriad axis=radio

#Need to reverse the order of the velocity axis
reorder in=Arp299co32.JCMTsub20.JyBEAMmiriad mode=12-3
out=Arp299co32.JCMTsub20.JyBEAMmiriad.reordered

###Export the prepared JCMT data cube into a fits file
fits in=Arp299co32.JCMTsub20.JyBEAMmiriad.reordered op=xyout
out=Arp299co32.JCMTsub20.JyBEAM.fits
```

For the SMA data, we first continuum subtracted the *uv* data set using the task `uvlin`. In order to use this task, we determined which channels are emission line free. In order to get a dirty mosaic map, we used the `invert` task. The dirty mosaic map was binned to 20 km/s starting at -390.11 km/s and a robust weighting scheme was used to get a good balance of resolution and sensitivity. The `mossdi` task was used to get a clean model and then the `restor` task to convolve the clean model with the beam to obtain the clean mosaic map. We implemented a 2σ cutoff to the clean model in order not to clean too deeply. The `mossen` task is used to obtain a gain map in order to correct the clean map for the primary beam pattern. The JCMT map is regridded to match the SMA map and the two maps are combined using the

`immerge` task. The following is the procedure used to prepare the SMA map and combine it with the JCMT map:

```
uvlist vis=arp299f1_l.uv options=spectra
#window 2 starts at -760.818
#window 23 ends at 832.643
#velocity interval is 0.712
uvaver vis=arp299f1_l.uv  line=velocity,2239,-760.818,0.712,0.712
       out=arp299f1_l.uv.vel
uvaver vis=arp299f2_l.uv  line=velocity,2239,-760.818,0.712,0.712
       out=arp299f2_l.uv.vel

uvlin vis=arp299f1_l.uv.vel out=arp299f1_l.uv.nocont order=1
      chans=1,600,1639,2239 offset=-20.1,1.3
uvlin vis=arp299f2_l.uv.vel out=arp299f2_l.uv.nocont order=1
      chans=1,600,1639,2239 offset=-1.5,1.2

invert vis=arp299f1_l.uv.nocont,arp299f2_l.uv.nocont map=Arp299co32.im
       beam=Arp299co32.beam options=double,systemp,mosaic imsize=512
       cell=0.2arcsec robust=0.5 line=velocity,40,-390.1,20 sup=38
##Theoretical rms noise: 6.575E-02

#Check the created map
cgdisp in=Arp299co32.im device=/xs
#First 7 and last 4 channels noise. Use to determine rms
```

```
histo in=Arp299co32.im region="quarter(1,7)"
##Mean -3.603604E-05 Rms 3.53284E-02 Sum -1.94259E+01 (539070 points)
##Maximum value      1.346297E-01    at (172,341,6,1)
##Minimum value     -1.534902E-01    at (351,287,3,1)

histo in=Arp299co32.im region="quarter(36,40)"
##Mean -1.680603E-04 Rms    3.75209E-02 Sum  -6.47116E+01 (385050 points)
##Maximum value      1.757702E-01    at (301,337,37,1)
##Minimum value     -1.453050E-01    at (425,265,39,1)

#Take average as rms...3.64e-2
###Clean the image plane with a 2 sigma cutoff
mossdi map=Arp299co32.im beam=Arp299co32.beam out=Arp299co32.clean
      region=quarter niters=2000 cutoff=0.0728
restor map=Arp299co32.im beam=Arp299co32.beam model=Arp299co32.clean
      out=Arp299co32.map
#Using gaussian beam fwhm of    2.236 by    1.848 arcsec.
#Position angle:  -15.8 degrees.

###Correct for the primary beam
mossen in=Arp299co32.map gain=Arp299.map.gain sen=Arp299.map.sen
maths exp="Arp299co32.map/Arp299.map.gain" mask=Arp299.map.gain.gt.0.5
     out=Arp299co32.mapg1
```

Table A.1. Miriad SMA and SMA+JCMT Comparison

	SMA			SMA+JCMT		
Region	Maximum (Jy/beam)	Minimum (Jy/beam)	Flux (Jy km s^{-1})	Maximum (Jy/beam)	Minimum (Jy/beam)	Flux (Jy km s^{-1})
A	857.97	1.47	1350	888.49	1.46	1640
B	303.44	1.46	711	311.56	1.48	830
C	124.20	1.46	489	132.03	1.46	723

```
regrid in=Arp299.JCMT.JyBEAM.reorder.miriad
     out=Arp299.JCMT.JyBEAM.regrid.miriad axes=1,2,3 tin=Arp299co32.mapg1

immerge in=Arp299co32.mapg1,Arp299.JCMT.JyBEAM.regrid.miriad
     out=Arp299co32.feather.cube.miriad factor=1

moment in=Arp299co32.feather.cube.miriad region="quarter(8,35)" clip=0.0728
      out=Arp299co32.feather.mom0

moment in=Arp299co32.mapg1 region="quarter(8,35)" clip=0.0728
      out=Arp299co32.mapg1.mom0
```

A.2 CASA

In CASA (v3.2.1), the *uv* data set is Fourier transformed, cleaned and primary beam corrected within the one task `clean`. We started by importing

the SMA *uv* data sets into the CASA format and concatenate the sets into one file. The continuum is subtracted from the data using the `uvcontsub2` task, inputing the spectral windows that are line free (see Figure A.2) and assuming the continuum can be fit by a linear equation. The data is binned to 20 km/s starting at -390.1km/s to match the JCMT data cube. A robust weighting scheme was implemented as used in Miriad and a threshold of 2σ in order not to clean too deeply. The following procedure was taken in CASA:

```
os.system('mkdir arp299f1_ms_files')
myfiles=[]

for i in range(1,25):
        msfile="arp299f1_ms_file/arp299f1.spw"+str(i)+".ms"
        importuvfits(fitsfile="arp299f1_l.spwfits/arp299f1_1.spw"+str(i),
                     vis=msfile)
        myfiles.append(msfile)

os.system('mkdir arp299f2_ms_files')
myfiles2=[]

for i in range(1,25):
        msfile2="arp299f2_ms_file/arp299f2.spw"+str(i)+".ms"
        importuvfits(fitsfile="arp299f2_l.spwfits/arp299f2_1.spw"+str(i),
                     vis=msfile2)
        myfiles2.append(msfile2)
```

```
concat(vis=myfiles,concatvis="arp299f1.uv.ms",timesort=True)
concat(vis=myfiles2,concatvis="arp299f2.uv.ms",timesort=True)
concat(vis=["arp299f1.uv.ms","arp299f2.uv.ms"],concatvis="Arp299co32.uv.ms",
     timesort=True)

plotms(vis="Arp299co32.uv.ms",xaxis="freq",yaxis="amp",ydatacolumn="data",
     selectdata=True,coloraxis="spw",spw="0~23",averagedata=True,
     avgtime="99999",avgscan=T)

uvcontsub2(vis="Arp299co32.uv.ms",want_cont=T,combine='spw',
     fitspw='1~7:5~122,16~22:5~122',spw='',fitorder=1)

clean(vis="Arp299co32.uv.ms.contsub",imagename="Arp299co32.20",
     mode="velocity",start="-390.1kms",width="20kms",nchan=40,
     niter=1000,threshold="10mJy",ftmachine="ft",imagermode="mosaic",
     interactive=T,interpolation="nearest",imsize=512,cell="0.2arcsec",
     pbcor=T,weighting="briggs",robust=0.5)
#Beam used in restoration: 2.19338 by 1.87133 (arcsec) at pa -18.0679 (deg)
```

One issue with combining the JCMT and SMA maps in CASA is that the JCMT map does not have a fourth axis, the Stokes axis. CASA does not like to combine maps without the same number of axes, therefore we need to remove the Stokes axis from the SMA map or add one to the JCMT map. One way to remove the Stokes axis from the SMA map is to export it into a fits file with the

parameter `dropstokes` set to `True` and then import it back into CASA. The hope is that this "issue" will be fixed in upcoming versions. Another problem with CASA is that it doesn't import fits files from Starlink properly. We need to import and export the fits file in Miriad first. This however does not retain the beam information of the JCMT map when imported into CASA. We need to add this information back into the header. The two maps can be combined using the `feather` task without the need to regrid the JCMT map. After the combination, a integrated intensity map is created using the channels with line emission and pixels greater than 2σ. The following is the full procedure taken in CASA:

```
exportfits(imagename="Arp299co32.20.image",fitsimage="SMA.fits",dropstokes=T)
importfits(fitsimage="SMA.fits",imagename="Arp299co32.20.image.nostokes")


imhead(imagename="Arp299.JCMT.JyBEAM.image",mode="put",hdkey="beammajor",
     hdvalue="14arcsec")
imhead(imagename="Arp299.JCMT.JyBEAM.image",mode="put",hdkey="beamminor",
     hdvalue="14arcsec")
imhead(imagename="Arp299.JCMT.JyBEAM.image",mode="put",hdkey="beampa",
     hdvalue="0deg")

feather(imagename="Arp299.feather.cube",highres="Arp299co32.20.image.nostokes",
     lowres="Arp299.JCMT.JyBEAM.image")
```

Table A.2. CASA SMA and SMA+JCMT Comparison

	SMA			SMA+JCMT		
Region	Maximum (Jy/beam)	Minimum (Jy/beam)	Flux (Jy km s^{-1})	Maximum (Jy/beam)	Minimum (Jy/beam)	Flux (Jy km s^{-1})
A	872.56	1.36	1464	892.32	1.38	1693
B	307.86	1.36	745	306.63	1.36	773
C	138.90	1.36	629	138.95	1.36	775

```
imstat(imagename="Arp299.feather.cube",chans="0~7",box="111,204,274,319")
 #'rms': array([ 0.03409981]),

immoments imagename="Arp299.feather.cube",outfile="Arp299.feather.mom0",
     moments=[0],axis="spectral",chans="7~35",includepix=[0.068,10000]
```

The main goal of combining single dish and interferometric data is to remove the negative bowls by adding the missing flux due to the short spacing problem. We see that the feathering technique does not recover all the missing flux (there still exists negative flux; only 67% of flux from JCMT recovered) but it does a fairly good job at removing the negative bowls near the main sources of emission in Arp 299 using both Miriad and CASA. However, we do see differences in the two reduction packages. Comparing the peak values of each region in Arp 299 from Table A.1 and Table A.2, we see that the values differ before and after combination. This may be because the robust weighting scheme may differ from each package. However, we do see that the rms values and the beam used in restoration are similar. Comparing Figure A.1(b) and

A.3(b), the feathered maps, we do notice some differences. The region north-east of IC 694 is mostly recovered using CASA but with Miriad we still see some of major negative bowls remaining. This may indicate that the task in Miriad adds more flux around regions with positive flux while CASA attempts to disperse the flux uniformly in the map.

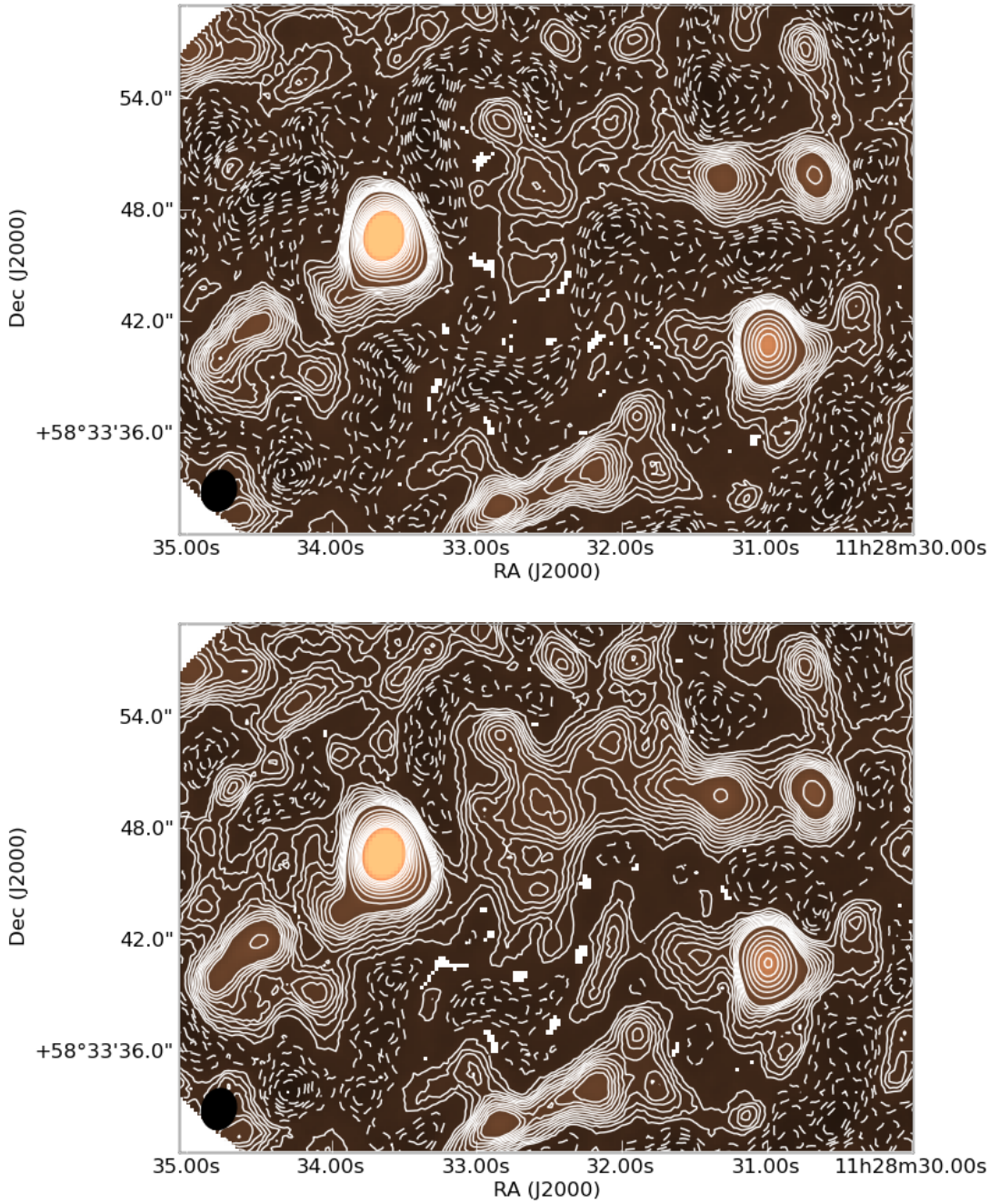

Figure A.1 Integrated intensity maps created using Miriad for ^{12}CO J=3-2:(*top*) SMA-only map, (*bottom*) Feathered map. The contour levels are -10, -9,..., 9, 10, 15, 20, 25, 30, 35, 40, 45, 50 times 2σ (=7.3 Jy/beam km/s). The dashed contours indicate missing flux. The white patches spread across the map indicate masked out pixels that are below 2σ. The black ellipse in the bottom left corner is the synthesized beam size.

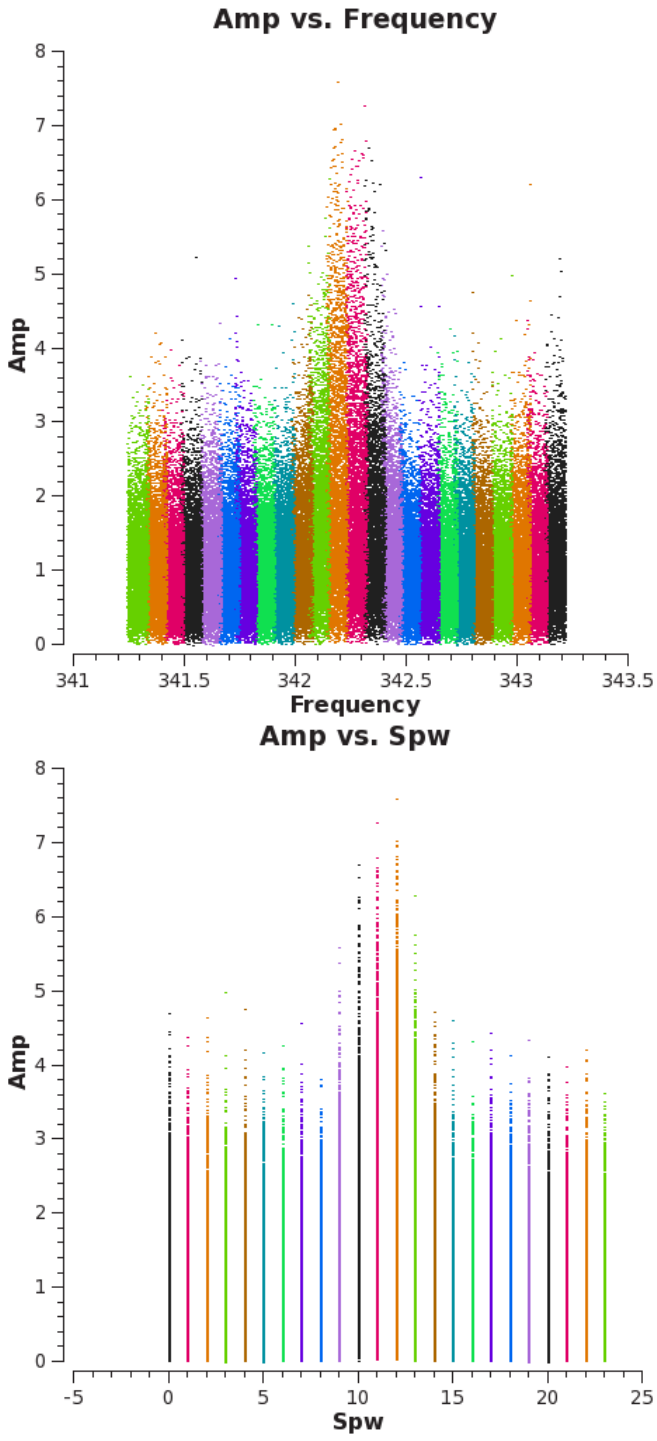

Figure A.2 (*top*): Amplitude versus Frequency plot for ^{12}CO J=3-2. The CO line is prominent.; (*bottom*): Amplitude versus Spectral Window plot for ^{12}CO J=3-2. The CO line is contained with spectral windows 8-15.

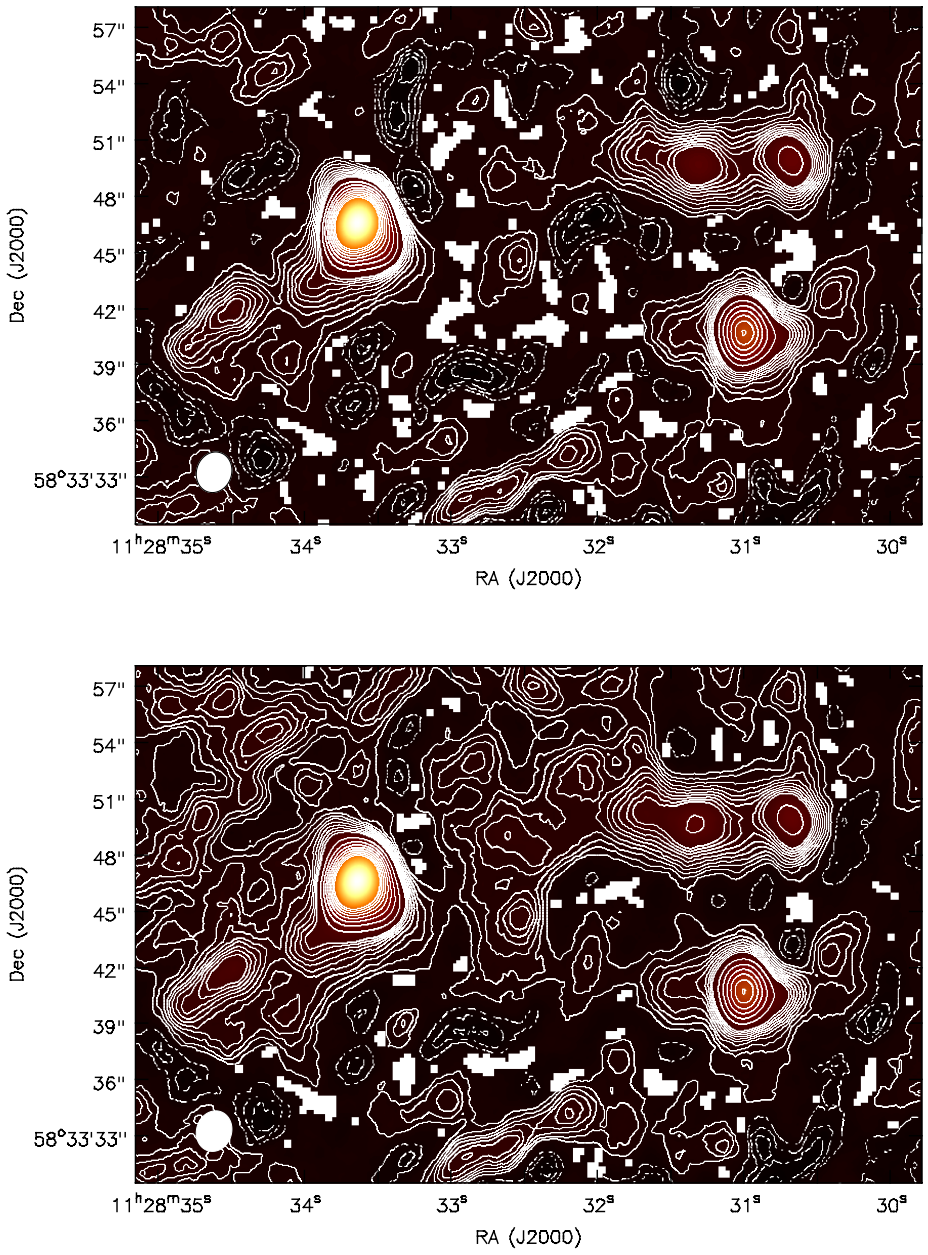

Figure A.3 Integrated intensity maps created using CASA for ^{12}CO J=3-2: (*top*) SMA-only map, (*bottom*) Feathered map. The contour levels are -10, -9,..., 9, 10, 15, 20, 25, 30, 35, 40, 45, 50 times 2σ (=7.3 Jy/beam km/s). The dashed contours indicate missing flux. The white patches spread across the map indicate masked out pixels that are below 2σ. The white ellipse in the bottom left corner is the synthesized beam size.

Appendix B

RADEX

RADEX (van der Tak et al., 2007) is a one-dimenional non-local thermal equilibrium (LTE) statistical radiative transfer code. It was originally written by John Black with improvements made in Leiden. The code uses the escape probability formulation assuming an isothermal and homogeneous medium without large-scale velocity fields. Since the code assumes a homogeneous medium, it does not know anything about the geometry or velocity fields. It also does not know if the escape probability assumption holds true. This code is similar to the large velocity gradient (LVG) method and provides a simple way to constrain physical conditions such as density and kinetic temperature using observational data.

B.1 Escape Probability

The probability that the photon will escape the medium from where it was created, β, depends only on the optical depth τ. RADEX offers the user a choice of three different escape probabilities for specific geometry assumptions.

The first is the expression used for an expanding spherical shell also known as the LVG approximation,

$$\beta_{LVG} = \frac{1}{\tau}\int_0^\tau e^{-\tau'}\,d\tau' = \frac{1-e^{-\tau}}{\tau}. \tag{B.1}$$

The second is for the case of a static, homogenous spherically symmetric medium given by

$$\beta_{sphere} = \frac{1.5}{\tau}\left[1 - \frac{2}{\tau^2} + \left(\frac{2}{\tau} + \frac{2}{\tau^2}\right)e^{-\tau}\right]. \tag{B.2}$$

The third is for a plane-parallel "slab" geometry, applicable to shocks given by

$$\beta_{slab} = \frac{1-e^{-3\tau}}{3\tau} \tag{B.3}$$

Figure B.1 taken from van der Tak et al. (2007) shows the behaviour of β as a function of τ for comparison. For our analysis we use the LVG approximation escape probability. This will enable us to compare our results with previous LVG modeling

B.2 Capabilities

For a homogeneous medium, the optical depth is given by

$$\tau = \frac{c^3}{8\pi\nu_{ul}^3}\frac{A_{ul}N_{mol}}{1.064\Delta V}\left[x_l\frac{g_u}{g_l} - x_u\right] \tag{B.4}$$

where A_{ul} is the Einstein coefficient for spontaneous emission, N_{mol} is the molecular column density, ΔV is the full width half-maximum (FWHM) in velocity units, x_i is the fraction population of level i and g_i is the statistical weight of level i. RADEX takes the following inputs:

- The molecule required for modeling

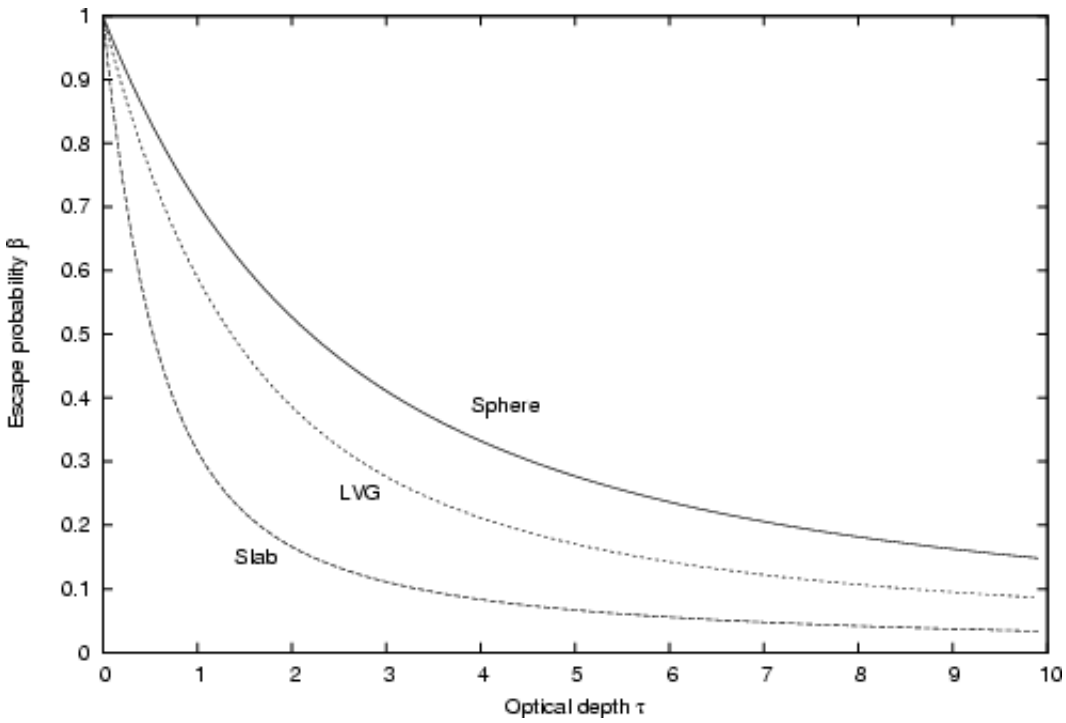

Figure B.1 Escape probability β as a function of τ taken from van der Tak et al. (2007) for different geometries: uniform sphere (solid line), expanding sphere (LVG; dotted line) and plane-parallel slab (dashed line).

- The name of the output file
- Spectral range of the required transition lines for the output in GHz
- The blackbody temperature of the background radiation field (taken to be T_{CBR} =2.73K)
- The kinetic temperature of the molecular cloud in K
- The number density of the collisional partner (in most cases H_2) in cm^{-3}
- The column density of the molecule in cm^{-2}

- The FWHM of the line in km s^{-1}; assumed the same for all transition lines

The output file contains the inputs from the user and the radiative transfer solution which includes:

- The excitation temperature of the molecule (K)
- The optical depth, τ at the line center
- T_R. the Rayleigh-Jeans equivalent of the intensity of the line with the background subtracted; this is the value that is observed by the telescope.
- The upper and lower population levels
- The flux in units of K km s^{-1} and erg cm^{-2} s^{-1}.

Figure B.2 shows a sample output for two RADEX runs which show that runs with the same N/dV values result in the same output. For the ratio values, we make use of the flux in K km s^{-1}.

```
* Radex version        : 20nov08
* Geometry             : Expanding sphere
* Molecular data file  : /home/sliwak/Radex/data/12co.dat
* T(kin)            [K]:   20.000
* Density of H2  [cm-3]:  1.000E+04
* Density of pH2 [cm-3]:  9.982E+03
* Density of oH2 [cm-3]:  1.774E+01
* T(background)     [K]:    2.730
* Column density [cm-2]:  1.000E+15
* Line width     [km/s]:    1.000
Calculation finished in   18 iterations
      LINE         E_UP       FREQ        WAVEL     T_EX      TAU        T_R
      POP        POP       FLUX        FLUX
                   (K)        (GHz)       (um)      (K)                  (K)
                   UP        LOW      (K*km/s) (erg/cm2/s)
1      -- 0          5.5    115.2712   2600.7576   24.059  5.061E-02  1.015E+00
4.133E-01  1.734E-01  1.080E+00  2.130E-08
2      -- 1         16.6    230.5380   1300.4037   13.495  2.189E-01  1.674E+00
3.035E-01  4.133E-01  1.782E+00  2.812E-07
3      -- 2         33.2    345.7960    866.9634   10.973  2.014E-01  8.490E-01
9.363E-02  3.035E-01  9.037E-01  4.812E-07
* Radex version        : 20nov08
* Geometry             : Expanding sphere
* Molecular data file  : /home/sliwak/Radex/data/12co.dat
* T(kin)            [K]:   20.000
* Density of H2  [cm-3]:  1.000E+04
* Density of pH2 [cm-3]:  9.982E+03
* Density of oH2 [cm-3]:  1.774E+01
* T(background)     [K]:    2.730
* Column density [cm-2]:  1.000E+17
* Line width     [km/s]:  100.000
Calculation finished in   18 iterations
      LINE         E_UP       FREQ        WAVEL     T_EX      TAU        T_R
      POP        POP       FLUX        FLUX
                   (K)        (GHz)       (um)      (K)                  (K)
                   UP        LOW      (K*km/s) (erg/cm2/s)
1      -- 0          5.5    115.2712   2600.7576   24.059  5.061E-02  1.015E+00
4.133E-01  1.734E-01  1.080E+02  2.130E-06
2      -- 1         16.6    230.5380   1300.4037   13.495  2.189E-01  1.674E+00
3.035E-01  4.133E-01  1.782E+02  2.812E-05
3      -- 2         33.2    345.7960    866.9634   10.973  2.014E-01  8.490E-01
9.363E-02  3.035E-01  9.037E+01  4.812E-05
```

Figure B.2 Sample output from two RADEX runs with T_{kin} =20 K and density of H_2=10^4 cm^{-3}. The first run has a column density of $N(^{12}CO) = 10^{15}$ cm^{-2} and line width dV=1 km s^{-1}. The second run has a column density of $N(^{12}CO)$ = 10^{17} cm^{-2} and line width dV=100 km s^{-1}. Both runs have the same N/dV values which result in the same output.

Bibliography

Aalto, S., Booth, R. S., Black, J. H., & Johansson, L. E. B. 1995, A&A, 300, 369

Aalto, S., Radford, S. J. E., Scoville, N. Z., & Sargent, A. I. 1997, ApJ, 475, L107+

Alonso-Herrero, A., Rieke, G. H., Colina, L., Pereira-Santaella, M., García-Marín, M., Smith, J.-D. T., Brandl, B., Charmandaris, V., & Armus, L. 2009, ApJ, 697, 660

Alonso-Herrero, A., Rieke, G. H., Rieke, M. J., Colina, L., Pérez-González, P. G., & Ryder, S. D. 2006, ApJ, 650, 835

Alonso-Herrero, A., Rieke, G. H., Rieke, M. J., & Scoville, N. Z. 2000, ApJ, 532, 845

Armus, L., Heckman, T., & Miley, G. 1987, AJ, 94, 831

Barnes, J. E. & Hernquist, L. E. 1991, ApJ, 370, L65

Calzetti, D., Kennicutt, R. C., Engelbracht, C. W., Leitherer, C., Draine, B. T., Kewley, L., Moustakas, J., Sosey, M., Dale, D. A., Gordon, K. D., Helou, G. X., Hollenbach, D. J., Armus, L., Bendo, G., Bot, C., Buckalew, B., Jarrett, T., Li, A., Meyer, M., Murphy, E. J., Prescott, M., Regan, M. W., Rieke, G. H., Roussel, H., Sheth, K., Smith, J. D. T., Thornley, M. D., & Walter, F. 2007, ApJ, 666, 870

Casoli, F., Combes, F., Augarde, R., Figon, P., & Martin, J. M. 1989, A&A, 224, 31

Casoli, F., Dupraz, C., & Combes, F. 1992, A&A, 264, 55

Casoli, F., Willaime, M.-C., Viallefond, F., & Gerin, M. 1999, A&A, 346, 663

Charmandaris, V., Laurent, O., Le Floc'h, E., Mirabel, I. F., Sauvage, M., Madden, S. C., Gallais, P., Vigroux, L., & Cesarsky, C. J. 2002a, A&A, 391, 429

Charmandaris, V., Stacey, G. J., & Gull, G. 2002b, ApJ, 571, 282

Currie, M. J., Draper, P. W., Berry, D. S., Jenness, T., Cavanagh, B., & Economou, F. 2008, in Astronomical Society of the Pacific Conference Series, Vol. 394, Astronomical Data Analysis Software and Systems XVII, ed. R. W. Argyle, P. S. Bunclark, & J. R. Lewis, 650–+

Daddi, E., Elbaz, D., Walter, F., Bournaud, F., Salmi, F., Carilli, C., Dannerbauer, H., Dickinson, M., Monaco, P., & Riechers, D. 2010, ApJ, 714, L118

Dickman, R. L., Snell, R. L., & Schloerb, F. P. 1986, ApJ, 309, 326

Downes, D. & Solomon, P. M. 1998, ApJ, 507, 615

Downes, D., Solomon, P. M., & Radford, S. J. E. 1993, ApJ, 414, L13

Gao, Y. & Solomon, P. M. 2004, ApJ, 606, 271

Genzel, R., Lutz, D., Sturm, E., Egami, E., Kunze, D., Moorwood, A. F. M., Rigopoulou, D., Spoon, H. W. W., Sternberg, A., Tacconi-Garman, L. E., Tacconi, L., & Thatte, N. 1998, ApJ, 498, 579

Genzel, R., Tacconi, L. J., Gracia-Carpio, J., Sternberg, A., Cooper, M. C., Shapiro, K., Bolatto, A., Bouché, N., Bournaud, F., Burkert, A., Combes, F., Comerford, J., Cox, P., Davis, M., Schreiber, N. M. F., Garcia-Burillo, S., Lutz, D., Naab, T., Neri, R., Omont, A., Shapley, A., & Weiner, B. 2010, MNRAS, 407, 2091

Graciá-Carpio, J., García-Burillo, S., Planesas, P., Fuente, A., & Usero, A. 2008, A&A, 479, 703

Heckman, T. M., Armus, L., Weaver, K. A., & Wang, J. 1999, ApJ, 517, 130

Hibbard, J. E. & Yun, M. S. 1999, AJ, 118, 162

Higdon, S. J. U., Armus, L., Higdon, J. L., Soifer, B. T., & Spoon, H. W. W. 2006, ApJ, 648, 323

Hinz, J. L. & Rieke, G. H. 2006, ApJ, 646, 872

Ho, P. T. P., Moran, J. M., & Lo, K. Y. 2004, ApJ, 616, L1

Hummer, D. G. & Storey, P. J. 1987, MNRAS, 224, 801

Jones, T. J., Gehrz, R. D., & Smith, J. 1990, AJ, 99, 1470

Kawamura, A., Mizuno, Y., Minamidani, T., Filipović, M. D., Staveley-Smith, L., Kim, S., Mizuno, N., Onishi, T., Mizuno, A., & Fukui, Y. 2009, ApJS, 184, 1

Kennicutt, Jr., R. C. 1998, ARA&A, 36, 189

McKee, C. F. & Ostriker, E. C. 2007, ARA&A, 45, 565

Menéndez-Delmestre, K., Blain, A. W., Smail, I., Alexander, D. M., Chapman, S. C., Armus, L., Frayer, D., Ivison, R. J., & Teplitz, H. 2009, ApJ, 699, 667

Murphy, Jr., T. W., Armus, L., Matthews, K., Soifer, B. T., Mazzarella, J. M., Shupe, D. L., Strauss, M. A., & Neugebauer, G. 1996, AJ, 111, 1025

Nakagawa, T., Nagata, T., Geballe, T. R., Okuda, H., Shibai, H., & Matsuhara, H. 1989, ApJ, 340, 729

Neff, S. G., Ulvestad, J. S., & Teng, S. H. 2004, ApJ, 611, 186

Panuzzo, P., Rangwala, N., Rykala, A., Isaak, K. G., Glenn, J., Wilson, C. D., Auld, R., Baes, M., Barlow, M. J., Bendo, G. J., Bock, J. J., Boselli, A., Bradford, M., Buat, V., Castro-Rodríguez, N., Chanial, P., Charlot, S., Ciesla, L., Clements, D. L., Cooray, A., Cormier, D., Cortese, L., Davies, J. I., Dwek, E., Eales, S. A., Elbaz, D., Fulton, T., Galametz, M., Galliano, F., Gear, W. K., Gomez, H. L., Griffin, M., Hony, S., Levenson, L. R., Lu, N., Madden, S., O'Halloran, B., Okumura, K., Oliver, S., Page, M. J., Papageorgiou, A., Parkin, T. J., Pérez-Fournon, I., Pohlen, M., Polehampton, E. T., Rigby, E. E., Roussel, H., Sacchi, N., Sauvage, M., Schulz, B., Schirm, M. R. P., Smith, M. W. L., Spinoglio, L., Stevens, J. A., Srinivasan, S., Symeonidis, M., Swinyard, B., Trichas, M., Vaccari, M., Vigroux, L., Wozniak, H., Wright, G. S., & Zeilinger, W. W. 2010, A&A, 518, L37+

Pérez-Torres, M. A., Alberdi, A., Romero-Cañizales, C., & Bondi, M. 2010, A&A, 519, L5+

Petitpas, G. R. & Wilson, C. D. 2000, ApJ, 538, L117

Puget, J. L. & Leger, A. 1989, ARA&A, 27, 161

Rangwala, N., Maloney, P. R., Glenn, J., Wilson, C. D., Rykala, A., Isaak, K., Baes, M., Bendo, G. J., Boselli, A., Bradford, C. M., Clements, D. L., Cooray, A., Fulton, T., Imhof, P., Kamenetzky, J., Madden, S. C., Mentuch, E., Sacchi, N., Sauvage, M., Schirm, M. R. P., Smith, M. W. L., Spinoglio, L., & Wolfire, M. 2011, ArXiv e-prints

Roche, P. F., Aitken, D. K., Smith, C. H., & Ward, M. J. 1991, MNRAS, 248, 606

Rybicki, G. B. & Lightman, A. P. 1979, Radiative processes in astrophysics, ed. Rybicki, G. B. & Lightman, A. P.

Sanders, D. B., Mazzarella, J. M., Kim, D.-C., Surace, J. A., & Soifer, B. T. 2003, AJ, 126, 1607

Sanders, D. B. & Mirabel, I. F. 1996, ARA&A, 34, 749

Sanders, D. B., Scoville, N. Z., Young, J. S., Soifer, B. T., Schloerb, F. P., Rice, W. L., & Danielson, G. E. 1986, ApJ, 305, L45

Sargent, A. & Scoville, N. 1991, ApJ, 366, L1

Sault, R. J., Teuben, P. J., & Wright, M. C. H. 1995, in Astronomical Society of the Pacific Conference Series, Vol. 77, Astronomical Data Analysis Software and Systems IV, ed. R. A. Shaw, H. E. Payne, & J. J. E. Hayes, 433–+

Scoville, N. Z., Sargent, A. I., Sanders, D. B., & Soifer, B. T. 1991, ApJ, 366, L5

Scoville, N. Z., Yun, M. S., & Bryant, P. M. 1997, ApJ, 484, 702

Solomon, P. M., Downes, D., & Radford, S. J. E. 1992, ApJ, 387, L55

Solomon, P. M. & Vanden Bout, P. A. 2005, ARA&A, 43, 677

Stanford, S. A. & Wood, D. O. S. 1989, ApJ, 346, 712

Strong, A. W., Bloemen, J. B. G. M., Dame, T. M., Grenier, I. A., Hermsen, W., Lebrun, F., Nyman, L.-A., Pollock, A. M. T., & Thaddeus, P. 1988, A&A, 207, 1

Sugai, H., Davies, R. I., Malkan, M. A., McLean, I. S., Usuda, T., & Ward, M. J. 1999, ApJ, 527, 778

Tielens, A. G. G. M. 2005, The Physics and Chemistry of the Interstellar Medium, ed. Tielens, A. G. G. M.

van der Tak, F. F. S., Black, J. H., Schöier, F. L., Jansen, D. J., & van Dishoeck, E. F. 2007, A&A, 468, 627

Vigroux, L., Audouze, J., & Lequeux, J. 1976, A&A, 52, 1

Wilson, C. D., Petitpas, G. R., Iono, D., Baker, A. J., Peck, A. B., Krips, M., Warren, B., Golding, J., Atkinson, A., Armus, L., Cox, T. J., Ho, P., Juvela, M., Matsushita, S., Mihos, J. C., Pihlstrom, Y., & Yun, M. S. 2008, ApJS, 178, 189

Wilson, C. D. & Scoville, N. 1990, ApJ, 363, 435

Wilson, C. D., Walker, C. E., & Thornley, M. D. 1997, ApJ, 483, 210

Zezas, A., Ward, M. J., & Murray, S. S. 2003, ApJ, 594, L31

Zezas, A. L., Georgantopoulos, I., & Ward, M. J. 1998, MNRAS, 301, 915